



1D/3D trepang-like N-modified carbon confined bimetal carbides and metal cobalt: Boosting electron transfer via dual Mott-Schottky heterojunctions triggered built-in electric fields for efficient hydrogen evolution and tri-iodide reduction

Dan Qiao, Sining Yun^{*}, Menglong Sun, Jiaoe Dang, Yongwei Zhang, Shuangxi Yuan, Guangping Yang, Tianxiang Yang, Zan Gao, Zhiguo Wang

Functional Materials Laboratory (FML), School of Materials Science and Engineering, Xi'an University of Architecture and Technology, Xi'an, Shaanxi, 710055, China

ARTICLE INFO

Keywords:

Hydrogen evolution reaction
Dual Mott-Schottky heterojunctions
Triiodide reduction reaction
Electron transfer highway
Built-in electric field
Dye-sensitized solar cell
Counter electrode

ABSTRACT

Tailoring the electronic structure of active centres is a critical strategy for improving the activity of catalysts, but its implementation still remains challenging. Herein, advanced 1D/3D trepang-like N-modified carbon confined Co and $\text{Co}_6\text{Mo}_6\text{C}_2$ nanoparticles (namely $\text{Co}_6\text{Mo}_6\text{C}_2/\text{Co}@\text{NC}$), a dual Mott-Schottky heterojunctions catalyst, is elaborately fabricated by utilizing bimetallic-ZIF and phosphomolybdic acid hydrate. The robust built-in electric field triggered by the dual Mott-Schottky heterojunctions composed of the $\text{Co}_6\text{Mo}_6\text{C}_2$ and Co with N-modified carbon contact interfaces ($\text{Co}_6\text{Mo}_6\text{C}_2|\text{NC}$ and $\text{Co}|\text{NC}$) is favorable for transferring electrons and optimizing the electronic structures of the active centres near the $\text{Co}_6\text{Mo}_6\text{C}_2|\text{NC}$ and $\text{Co}|\text{NC}$ interfaces. The 1D/3D $\text{Co}_6\text{Mo}_6\text{C}_2/\text{Co}@\text{NC}$ achieves a small Tafel slope of 58 mV dec^{-1} . The photovoltaic device assembled with the $\text{Co}_6\text{Mo}_6\text{C}_2/\text{Co}@\text{NC}$ delivers a power conversion efficiency of 8.45 %. This work not only provides a new avenue for synthesizing high-performance carbon-confined metal and carbide electrocatalysts but also offers valuable insights into the synergistic effect of dual Mott-Schottky heterojunctions.

1. Introduction

Hydrogen evolution reaction (HER), oxygen evolution reaction (OER), and triiodide reduction reaction (IRR) are vital processes in energy conversion and storage technologies (e.g., solar cells, hydrogen production, fuel cells, etc.), but are still limited by slow reaction kinetics [1,2]. Electrode catalyst plays a critical role in enhancing the overall efficiency of electrochemical reaction. Take counter electrode of solar cell as an example, it not only accepts the electron from external circuit but also adsorbs key reactants for IRR, which determine the final power energy conversion efficiency of photovoltaic devices [3–6]. Noble group metals including Pt, Pd, and Ru, have been regarded to exhibit superior catalytic activity for accelerating these processes; however, rarity and exorbitant cost restrict their large-scale availability [7,8]. Transition metals (TMs: Co, Mo, W) and transition metal carbides (TMCs), such as TaC [9], WC [10], and Mo_2C [11], have attracted enormous interest as potential substitutes because their abundance and low cost, and the similar electron structure to noble metal. Nevertheless, numerous

studies have indicated that TMs and TMCs exhibit non-ideal catalytic performance owing to the following reasons: i) Inevitable nanoparticle aggregation and coarsening during the high-temperature carbonization process ($\sim 900^\circ\text{C}$), resulting in insufficient contact between efficient active units and reactant intermediates. ii) Inappropriate adsorption/desorption energy of the active centres, attributed to their undesirable electronic structure. Hence, a strategy that simultaneously optimizes the reaction environment around the active sites of TMs or TMCs catalysts and regulates their electronic structure is urgently required.

In this respect, the integration of zeolitic imidazolate framework (ZIF)-derived three-dimensional (3D) porous N-modified carbon (NC) and TMs or TMCs nanoparticles to construct a graphitic layer-confined TMs or TMCs configuration is an effective method. On the one hand, ZIF-derived porous skeletons not only ensure the uniform dispersion of TMs or TMCs nanoparticles with the help of their spatial confinement effect but also protect the inner TMs or TMCs nanoparticles from electrolyte corrosion [12,13]. On the other hand, by taking advantage of the positive synergistic effect between ZIF-derived carbon matrix and TMs

^{*} Corresponding author.

E-mail addresses: yunsining@xauat.edu.cn, alexsyun1974@aliyun.com (S. Yun).

or TMCs, in which the former acts as conductive substance and the latter serve as active sites, the designed hybrid can achieve the better catalytic performance [14–16]. More significantly, the formed TMs|NC or TMCs|NC interfaces within the graphitic layer-confined TMs or TMCs configuration may promote electron transfer between different components via the Mott-Schottky effect, thereby inducing electron redistribution to form built-in electric fields and optimizing the electronic structure of the active centres to improve the desorption/adsorption ability of the reaction intermediates [17,18]. For example, Sun et al. synthesized a 1D/3D carbon-polyhedron comprising an NiCo|NC Mott-Schottky heterojunction. The NiCo|NC junction-driven electron transfer effectively improved the electronic state of the active units near the interface, leading to satisfactory IRR and HER activity [19]. Zhang et al. used WN-Ni nanoparticles encapsulated within N- and P-doped carbon nanotubes as a Mott-Schottky catalyst. Because of Mott-Schottky interface, efficient electronic pathways and electrophilic and nucleophilic regions were constructed, which effectively improved the catalytic performance [20]. Therefore, controlling the spontaneous electron transfer behavior to tailor the electronic structure of the active centres in Mott-Schottky catalysts is essential for enhancing the catalytic activity of the proposed catalysts.

Work function (W_f), a fundamental surface property of materials, is essential for controlling the electron flow, bending direction of energy band, and strength of the built-in electric field at the Mott-Schottky interface [21,22]. The difference in work function (ΔW_f), a Fermi-level difference between the metal and support, plays a key role in generating the interfacial driving force, which can highly regulate the strength of built-in electric field and electron transmit behavior between Mott-Schottky interfaces. For instance, Zhai et al. synthesized a series of Mott-Schottky catalysts using Pt and CoO (Co_3O_4 , CoO_x). Compared with Pt/CoO and Pt/ Co_3O_4 , Pt/ CoO_x exhibited the largest ΔW_f value, which made Pt/ CoO_x interface feature fast electron transfer ability and stronger built-in electric field that can modulate the electron density and adsorption capacity of active units more effectively [23]. Similarly, Ni et al. fabricated a heterojunction-containing catalyst using NiSe_2 and FeSe_2 ($\text{NiSe}_2/\text{FeSe}_2$), which had a larger ΔW_f than the $\text{CoSe}_2/\text{NiSe}_2$ heterojunction. A larger ΔW_f induces more charge redistribution into $\text{NiSe}_2/\text{FeSe}_2$, leading to better catalytic activity toward OER [24]. Altering ΔW_f via component conversion is a potent approach in controlling electron transfer behavior and regulating the electronic structure. However, this method still has significant limitations in ZIF-derived N-doped carbon-based catalysts with individual Mott-Schottky heterojunction; for example, metallic Co in Co-NC derived from Co-based ZIF is ideal active species for the alkaline HER, while the replacement of metallic Co with Co-based oxides to regulate ΔW_f and control electron transport may lead to undesirable results, such as a large overpotential and Tafel slope due to unsuitable oxygenophilic ability and poor conductivity of Co-based oxide active species [25]. Hence, novel electron transfer routes should be established in carbon-based Mott-Schottky catalysts to tackle these problems.

Based on the above, the work aims to fabricate a dual Mott-Schottky-type carbon-based catalyst and to probe the electron transfer behavior between dual Mott-Schottky interfaces. For this purpose, we designed 1D/3D trepan-like porous N-modified carbon-confined bimetal carbides and metal cobalt nanoparticles (denoted as $\text{Co}_6\text{Mo}_6\text{C}_2/\text{Co@NC}$), for the first time, as dual Mott-Schottky heterojunctions catalyst by employing bimetallic zeolitic imidazolate frameworks (BZIFs), phosphomolybdic acid hydrate (POM), and dicyandiamide as precursors. The $\text{Co}_6\text{Mo}_6\text{C}_2/\text{Co@NC}$ had several advantages, including the abundance of carbon nanotubes (CNTs), the upgraded channel structures, and a high degree of graphitization, which ensured an ideal reaction environment for active sites. Moreover, with the help of dual Mott-Schottky interfaces, the electronic structure of Co|NC was indirectly optimized by altering ΔW_f of the TMCs|NC. As a result, the $\text{Co}_6\text{Mo}_6\text{C}_2/\text{Co@NC}$ showed satisfactory catalytic activity and excellent durability for HER and IRR compared to $\text{Mo}_2\text{C}/\text{Co@NC}$ and achieved a small overpotential

(114 mV) at 10 mA cm^{-2} for water splitting and great power conversion efficiency (8.45 %) for solar cells.

2. Experimental section

2.1. Preparation of the ZnCo-BZIF

Initially, 2-methylimidazole (2-IM, 3.284 g, Aladdin 99 %) was dispersed in deionized water (DI water, 35 mL). The cetyltrimethylammonium bromide (CTAB, 15 mg, Aladdin 99 %), Co (NO_3) $_2$ ·6 H_2O (1.455 g, Aladdin 99 %), and $\text{Zn}(\text{NO}_3)_2$ ·6 H_2O (1.487 g, Aladdin 99 %) were dissolved in DI water (35 mL). The solutions were rapidly mixed and agitated for 2 h. After three washes and overnight drying at 60 °C, the ZnCo-BZIF powder was collected.

2.2. Preparation of the ZnCo-BZIF/POM

The prepared ZnCo-BZIF (0.20 g) powder was dispersed in methanol (65 mL) and stirred for 3 h. Phosphomolybdic acid hydrate (POM, 0.05 g, Aladdin 99 %) was then added to another solution containing methanol (35 mL) via ultrasonication. The POM and ZnCo-BZIF solutions were mixed at 100 °C for 6 h via a hydrothermal reaction. Finally, the samples were collected via centrifugation and placed in an oven overnight to obtain the desired product.

2.3. Synthesis of $\text{Co}_6\text{Mo}_6\text{C}_2/\text{Co@NC}$

ZnCo-BZIF/POM and dicyandiamide powders (with a mass ratio of 1:4) were placed in a tube furnace with ZnCo-BZIF/POM downstream. Afterward, the tube furnace was heated to 900 °C under N_2 at a 2 °C min^{-1} heating rate for 2 h. Upon natural cooling down, $\text{Co}_6\text{Mo}_6\text{C}_2/\text{Co@NC}$ was performed. For comparison, the as-obtained ZnCo-BZIF/POM was annealed without dicyandiamide at the afore mentioned conditions, denoted as $\text{Mo}_2\text{C}/\text{Co@NC}$. The ZnCo-BZIF was annealed without POM and dicyandiamide, denoted as Co@NC .

2.4. Fabrication of the HER electrodes

10 mg as-prepared electrocatalyst was dispersed in a solution comprising isopropyl alcohol and Nafion by ultrasonication over 30 min to acquire a mixed slurry. Next, the 90 μL of the prepared slurry was attached to the nickel foam (NF) (effective area of 1 cm^2) that had been soaked in HCl (1 M) solution. The HER catalyst loading was 0.90 mg cm^{-2} .

2.5. Fabrication of the IRR electrodes

In a typical photoanode fabrication process, purchased TiO_2 photoanodes (effective area of 0.16 cm^2) were annealed at 500 °C for 30 min, and when they cooled to approximately 120 °C–90 °C, the TiO_2 photoanodes were immediately placed in a reagent bottle containing N719 and immersed in the dark for one day. During the preparation of counter electrode, 80 mg electrode powder was added to 1 mL isopropyl alcohol solution and then ball milled with ZrO_2 pearls at 300 r min^{-2} for 4 h. The electrocatalyst was attached to fluorine-doped tin oxide (FTO) glass substrate and then sintered at 400 °C for 30 min to acquire the desired counter electrode. The typical Pt counter electrode was manufactured by annealing FTO glass substrate loaded with H_2PtCl_6 solution at 500 °C for 30 min. Finally, electrochemical tests were performed by adding one or two drops of I_3/T electrolyte in the gap of a symmetric cell with two counter electrodes.

2.6. Characterization

X-ray powder diffractometer (XRD, D/Max 2200, America), X-ray photoelectron spectroscopy (XPS, ASAP2020, Micromeritics, America),

Raman spectroscopy (LabRAM HR Evolution, Horiba, France), N_2 adsorption-desorption measurements (ASAP 2460, America), Brunauer-Emmett-Teller (BET) surface, and water contact angle (JC2000DM, China) were performed to analyze the structure and chemical component of as-prepared catalysts. Transmission electron microscopy and scanning transmission electron microscopy (STEM, FEI Tecnai F20, America), field emission scanning electron microscope (FESEM, ZEISS G500, Germany) coupled with Energy dispersion Spectrometer (EDS, X-Max 80T, Oxford Instruments, UK) were used to measure the structural characteristics and morphological features. An electrochemical analyzer (Chen-Hua, Shanghai, CHI 660E, China) recorded all electrochemical data including Tafel polarization and electrochemical impedance spectroscopy (EIS).

2.7. Electrochemical measurements

The three-electrode system consisting of working electrode (NF coated with catalyst), reference electrode (Hg/HgO electrode) and counter electrode (carbon rod) was used to evaluate the catalytic activity of the prepared samples in alkaline solution. Linear sweep voltammetry (LSV) test was made in the different potential scopes with the same sweep rate (5 mV s^{-1}) and all results were corrected for 95 % ohmic potential drop (iR) correction. From the corresponding LSV curve data, the Tafel slope was evaluated. In an alkaline solution, the relative potentials and the reversible hydrogen electrode (RHE) can be converted as follows: $E_{\text{RHE}} = E_{\text{Hg/HgO}} + 0.059 \cdot \text{pH} + 0.098$. Cyclic voltammetry (CV) curves were carried out to calculate the electrochemical double layer capacitance (C_{dl}) at different scanning speeds. The corresponding electrochemical surface area (ECSA) are estimated by the equation: $\text{ECSA} = C_{\text{dl}}/C_s$. Where C_s ($\sim 0.04 \text{ mF cm}^{-2}$) represents the specific

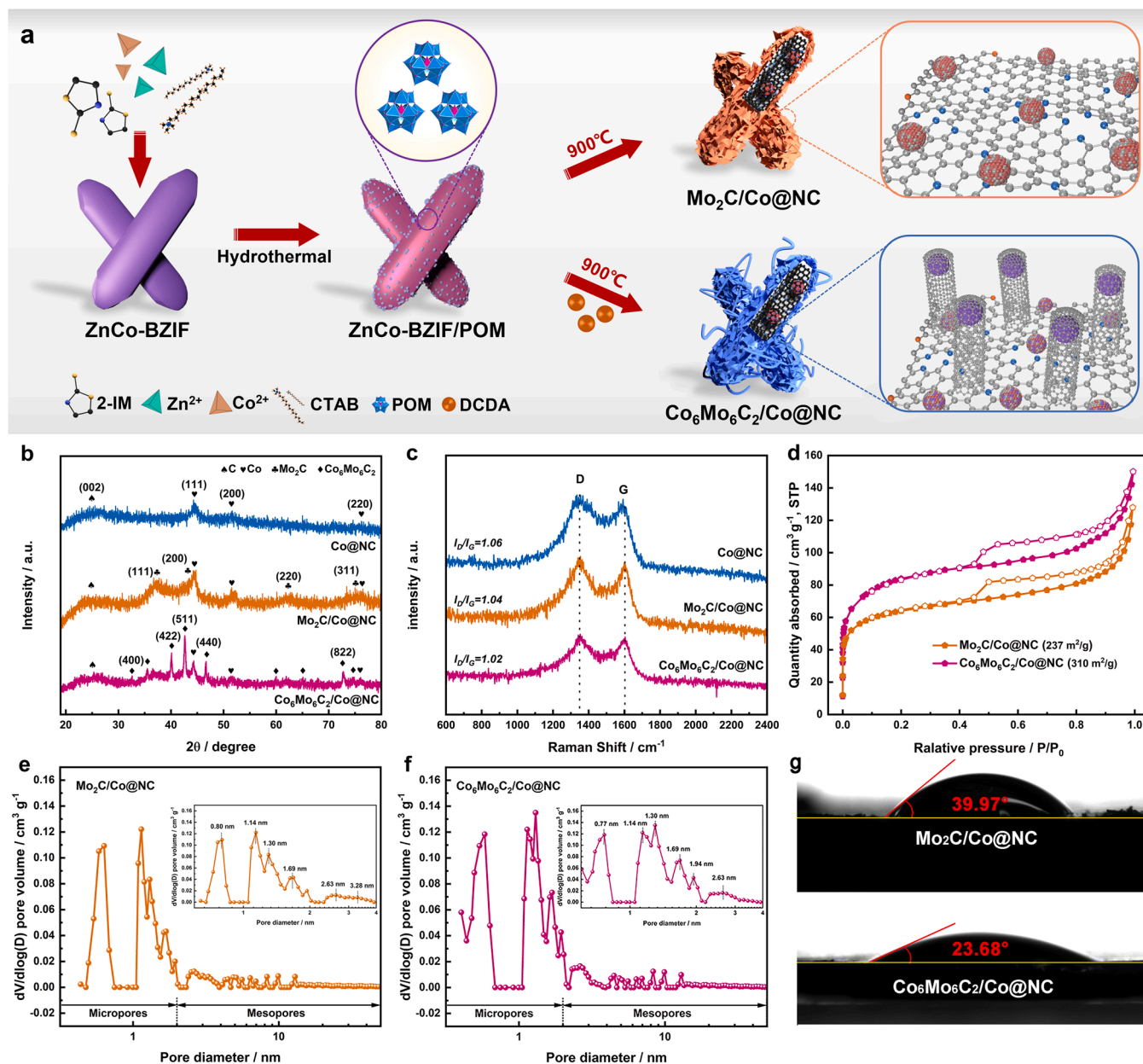


Fig. 1. (a) Synthesis route of the Mo₂C/Co@NC and Co₆Mo₆C₂/Co@NC. (b) XRD patterns and (c) Raman spectra of Co@NC, Mo₂C/Co@NC, and Co₆Mo₆C₂/Co@NC. (d) The N_2 adsorption-desorption isotherm of Mo₂C/Co@NC and Co₆Mo₆C₂/Co@NC and (e-f) the relative pore-size distribution curves. (g) Wettability test of Mo₂C/Co@NC and Co₆Mo₆C₂/Co@NC.

capacitance of the catalysts. Material stability was tested by testing LSV polarization curves before and after 1000 cycles and chronopotentiometry (CP) method in alkaline media.

The IRR properties of the prepared samples were evaluated in an iodine electrolyte (100 mM ClLiO_4 , 10 mM LiI , and 1 mM I_2). CV tests were performed in a three-electrode system consisting of an Pt electrode, a reference electrode (Ag/Ag^+), and a counter electrode. Photocurrent-voltage (J - V) curve was tested with the lighting conditions of AM 1.5G (100 mW cm^{-2}). The EIS measurement was tested in the frequency range (from 0.1 Hz to 1 MHz). Tafel polarization test was performed with a measurement voltage range of -0.8 to 0.8 V . Continuous CV operation (50 cycles) was used to test the stability of materials.

3. Results and discussion

3.1. Structure and morphology

The preparation process of the $\text{Mo}_2\text{C}/\text{Co@NC}$ and $\text{Co}_6\text{Mo}_6\text{C}_2/\text{Co@NC}$ is illustrated in Fig. 1a. Firstly, ZnCo-BZIF was prepared by adding structural guiding agent CTAB, metal ion, and 2-IM into DI water. Next, the ZnCo-BZIF powder was dispersed in methanol solution with POM for hydrothermal treatment to obtain a blue precipitate. After that, the dicyandiamide and blue precipitate were pyrolyzed at 900°C to obtain $\text{Co}_6\text{Mo}_6\text{C}_2/\text{Co@NC}$ catalyst (More detail can be seen in Experiment section).

In Fig. 1b, Co@NC , $\text{Mo}_2\text{C}/\text{Co@NC}$, and $\text{Co}_6\text{Mo}_6\text{C}_2/\text{Co@NC}$ exhibit the same diffraction peaks at approximately 44° , 51° , and 75° , corresponding to the (111), (200), and (220) faces of Co (JCPDS No. 15-0806). The broad peak at 24° represents the (002) lattice planes of graphitic carbon [26]. Besides, the diffraction patterns of $\text{Mo}_2\text{C}/\text{Co@NC}$ and $\text{Co}_6\text{Mo}_6\text{C}_2/\text{Co@NC}$ display the normal phase of Mo_2C (JCPDS No. 15-0457) and $\text{Co}_6\text{Mo}_6\text{C}_2$ (JCPDS No. 80-0339) respectively, confirming the coexistence of metallic Co and carbides (Mo_2C or $\text{Co}_6\text{Mo}_6\text{C}_2$) in the carbon skeletons. In Raman spectra (Fig. 1c), all samples display two distinctive characteristic peaks at around 1349 cm^{-1} (D band) and 1579 cm^{-1} (G band), reflecting the lattice disorder and graphitization degree of carbon matrix, respectively [27,28]. The value of I_D/I_G is 1.06, 1.04, and 1.02 for Co@NC , $\text{Mo}_2\text{C}/\text{Co@NC}$, and $\text{Co}_6\text{Mo}_6\text{C}_2/\text{Co@NC}$

respectively, suggesting $\text{Co}_6\text{Mo}_6\text{C}_2/\text{Co@NC}$ has greater graphitization degree, which is beneficial for electron transfer. The N_2 adsorption-desorption isotherms of $\text{Mo}_2\text{C}/\text{Co@NC}$ and $\text{Co}_6\text{Mo}_6\text{C}_2/\text{Co@NC}$ exhibit the type IV isotherm with H4 hysteresis loop, which proves the exist of micropores and mesoporous in carbon matrix (Fig. 1d). From the pore size distribution (Fig. 1e-f), $\text{Mo}_2\text{C}/\text{Co@NC}$ and $\text{Co}_6\text{Mo}_6\text{C}_2/\text{Co@NC}$ have numerous micropores located at approximately 1.14 nm , followed by mesopores ($\sim 2.63 \text{ nm}$). Previous literature has shown that micropores and mesopores could positively reduce the local electrical resistance and enrich the active site-electrolyte contact [29]. The BET surface area and pore volume of $\text{Co}_6\text{Mo}_6\text{C}_2/\text{Co@NC}$ are $310 \text{ m}^2/\text{g}$ and $0.16 \text{ cm}^3/\text{g}$ (Table S1), respectively, which are higher than those of $\text{Mo}_2\text{C}/\text{Co@NC}$ ($237 \text{ m}^2/\text{g}$ and $0.14 \text{ cm}^3/\text{g}$), meaning more exposed active sites in $\text{Co}_6\text{Mo}_6\text{C}_2/\text{Co@NC}$. In Fig. 1g, the contact angle of $\text{Co}_6\text{Mo}_6\text{C}_2/\text{Co@NC}$ (23.68°) is much smaller than that of $\text{Mo}_2\text{C}/\text{Co@NC}$ (39.97°), suggesting electrolyte is more likely to penetrate in $\text{Co}_6\text{Mo}_6\text{C}_2/\text{Co@NC}$ with good hydrophilicity. Notably, the good hydrophilicity of the catalyst facilitates the enhancement of the Volmer step by water molecules in the HER [30].

In Fig. 2a, the ZnCo-BZIFs exhibit a 3D foliated shape with a smooth surface, while the resulting Co@NC and $\text{Mo}_2\text{C}/\text{Co@NC}$ show a coarser surface (Fig. 2b-c). In contrast, the $\text{Co}_6\text{Mo}_6\text{C}_2/\text{Co@NC}$ reveal a trepang-like shape, in which 1D tentacle-like carbon nanotubes (CNTs) intertwine the surface of 3D carbon matrix (Fig. 2d). During carbonization, dicyandiamide started to convert N- and C-containing gases, enabling the directional growth of CNTs and the formation of $\text{Co}_6\text{Mo}_6\text{C}_2/\text{Co@NC}$ [31,32]. Elemental mapping analysis confirms that C, Co, N, and Mo are present in $\text{Co}_6\text{Mo}_6\text{C}_2/\text{Co@NC}$, as observed in Fig. 2e-f, which is in line with the result of XRD.

Fig. 3a-b further demonstrate that the trepang-like $\text{Co}_6\text{Mo}_6\text{C}_2/\text{Co@NC}$ consists of 1D tentacle-like CNTs and a 3D carbon matrix. On top of the CNTs, the nanoparticles are wrapped with a carbon layer approximately 3 nm thick, as shown in Fig. 3c. Fig. 3d suggests that the lattice-spacing of these encapsulated nanoparticles is 0.205 nm , corresponding to the (111) phase of metallic Co and the lattice-spacing of 0.360 nm corresponds to graphite carbon. In Fig. 3e, there are nanoparticles evenly embedded throughout the 3D carbon matrix and the SAED pattern (Fig. 3f) confirms that these tiny nanoparticles are Co and

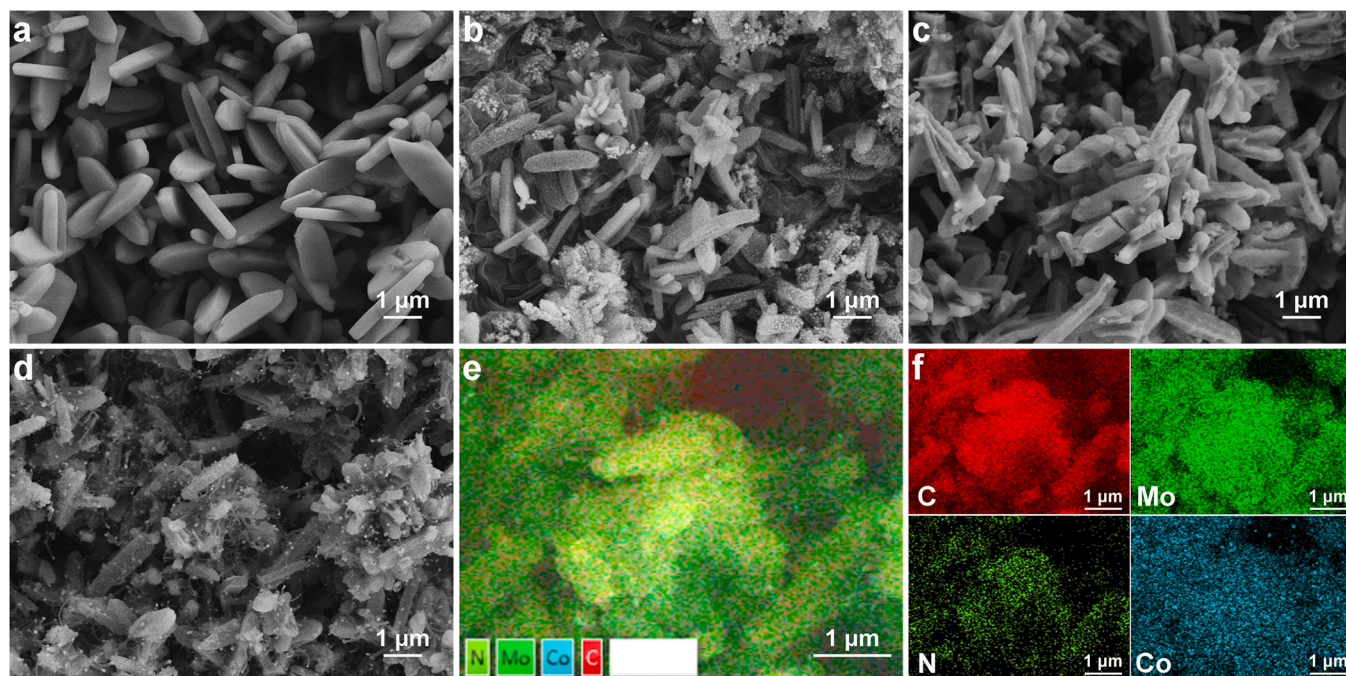


Fig. 2. SEM images of (a) ZnCo-BZIF, (b) Co@NC , (c) $\text{Mo}_2\text{C}/\text{Co@NC}$, and (d) $\text{Co}_6\text{Mo}_6\text{C}_2/\text{Co@NC}$. (e-f) Elemental mapping images of $\text{Co}_6\text{Mo}_6\text{C}_2/\text{Co@NC}$.

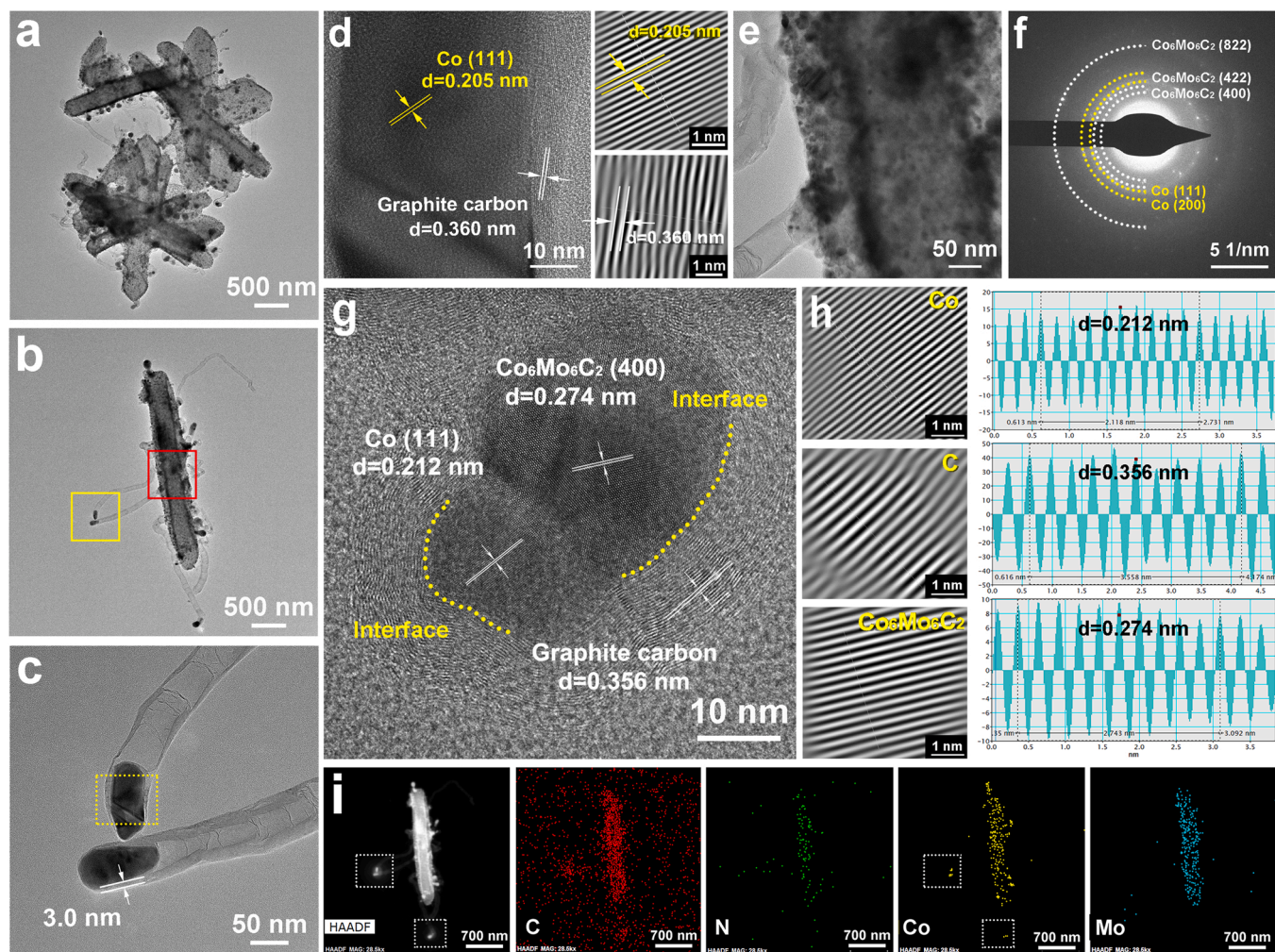


Fig. 3. (a–b) TEM images, (c) and local HRTEM image magnified from yellow solid line frame in (b). (d) The magnified HRTEM image of the yellow dashed box in (c) and the corresponding inverse fast fourier transform (IFFT) images, (e) HRTEM image magnified from the red solid line frame in (b), and (f) the corresponding SAED pattern. (g) HRTEM image and (h) the corresponding IFFT and line profile of IFFT images, (i) HAADF (high angle annular dark field) and elemental mapping images of $\text{Co}_6\text{Mo}_6\text{C}_2/\text{Co}@NC$ (dot line: nanoparticles of top of CNTs).

$\text{Co}_6\text{Mo}_6\text{C}_2$ species, which coincides with XRD results. Fig. 3g displays the typical carbon-confined nanoparticles structure, in which the lattice-spacing of 0.212, 0.274, and 0.356 nm represent the (111) crystal plane of Co, the (400) crystal plane of $\text{Co}_6\text{Mo}_6\text{C}_2$, and graphite carbon respectively (Fig. 3h). The formed graphite carbon confined Co and $\text{Co}_6\text{Mo}_6\text{C}_2$ nanoparticles configuration indicates that dual Mott-Schottky heterojunctions ($\text{Co}|NC$ and $\text{Co}_6\text{Mo}_6\text{C}_2|NC$) were successfully constructed in $\text{Co}_6\text{Mo}_6\text{C}_2/\text{Co}@NC$. Notably, $\text{Co}_6\text{Mo}_6\text{C}_2$ has metallic properties, which have been reported in the previously literatures [33,34]. The HAADF images and elemental mapping (Fig. 3i) depict the uniform C, N, Co, and Mo elements distribution in the 3D carbon support as well as the Co nanoparticles distribution on the top of the CNT (white dotted box).

The survey spectra (Fig. 4a) prove that C, N, and Co are presented in $\text{Co}@NC$, $\text{Mo}_2\text{C}/\text{Co}@NC$, and $\text{Co}_6\text{Mo}_6\text{C}_2/\text{Co}@NC$, while the Mo element only exists in $\text{Mo}_2\text{C}/\text{Co}@NC$ and $\text{Co}_6\text{Mo}_6\text{C}_2/\text{Co}@NC$. The C 1s spectrum of $\text{Co}_6\text{Mo}_6\text{C}_2/\text{Co}@NC$ in Fig. 4b shows three peaks including C-C/C=C (284.6 eV), C-N (285.2 eV), and C-O (288.3 eV). In Fig. 4c, there are four peaks of N 1s belonging to pyridinic-N (~399 eV), pyrrolic-N (~400 eV), graphitic-N (~401.5 eV), and oxidized-N (~402 eV) respectively. The details of the coordination between N and C are described in Fig. 4d. Among them, graphitic-N favors electrical conductivity and electron transfer, while pyridine-N is beneficial to improve catalytic activity [35]. Following the comparison in Table S2,

$\text{Co}_6\text{Mo}_6\text{C}_2/\text{Co}@NC$ has a higher proportion of graphitic-N and pyridine-N, which can be used as evidence for the good catalytic performance of $\text{Co}_6\text{Mo}_6\text{C}_2/\text{Co}@NC$. In Co 2p spectrum (Fig. 4e), the peaks located at 778.4 eV/793.8 eV and 780.0 eV/804.6 eV are attributed to Co^0 and Co^{2+} respectively, verifying the formation of metallic Co and Co-N bond [36,37]. The peaks of the Mo 3d spectrum (Fig. 4f) at 232.3 eV/235.4 eV and 229.8 eV/234.2 eV belong to Mo-based oxide (Mo^{6+} and Mo^{4+}), due to the aggregation of surface oxygen in the air [38,39]. The Mo^{2+} 3d_{5/2} and Mo^{2+} 3d_{3/2} peaks at 228.4 eV and 231.5 eV are involved in the Mo-C bonds, which are claimed as important active sites for electrocatalysis [11].

3.2. Electrochemical activity for HER

Fig. 5a depicts the LSV curves with iR correction for electrodes fabricated with carbon-based Mott-Schottky catalysts, standard Pt/C, and pure NF. $\text{Co}_6\text{Mo}_6\text{C}_2/\text{Co}@NC$ exhibits 114 mV at η_{10} , which is lower than $\text{Mo}_2\text{C}/\text{Co}@NC$ (159 mV), $\text{Co}@NC$ (190 mV), and NF (265 mV). In addition, $\text{Co}_6\text{Mo}_6\text{C}_2/\text{Co}@NC$ shows an overpotential of 152 mV at 200 mA cm⁻², less than $\text{Mo}_2\text{C}/\text{Co}@NC$ (193 mV) and $\text{Co}@NC$ (207 mV), confirming its good catalytic activity, as shown in Fig. S1a. The Tafel slope (Fig. 5b) derived from the LSV curve enable the evaluation of the HER kinetics. Compared with $\text{Mo}_2\text{C}/\text{Co}@NC$ (77 mV dec⁻¹), $\text{Co}@NC$ (152 mV dec⁻¹), and NF (181 mV dec⁻¹), the Tafel slope of

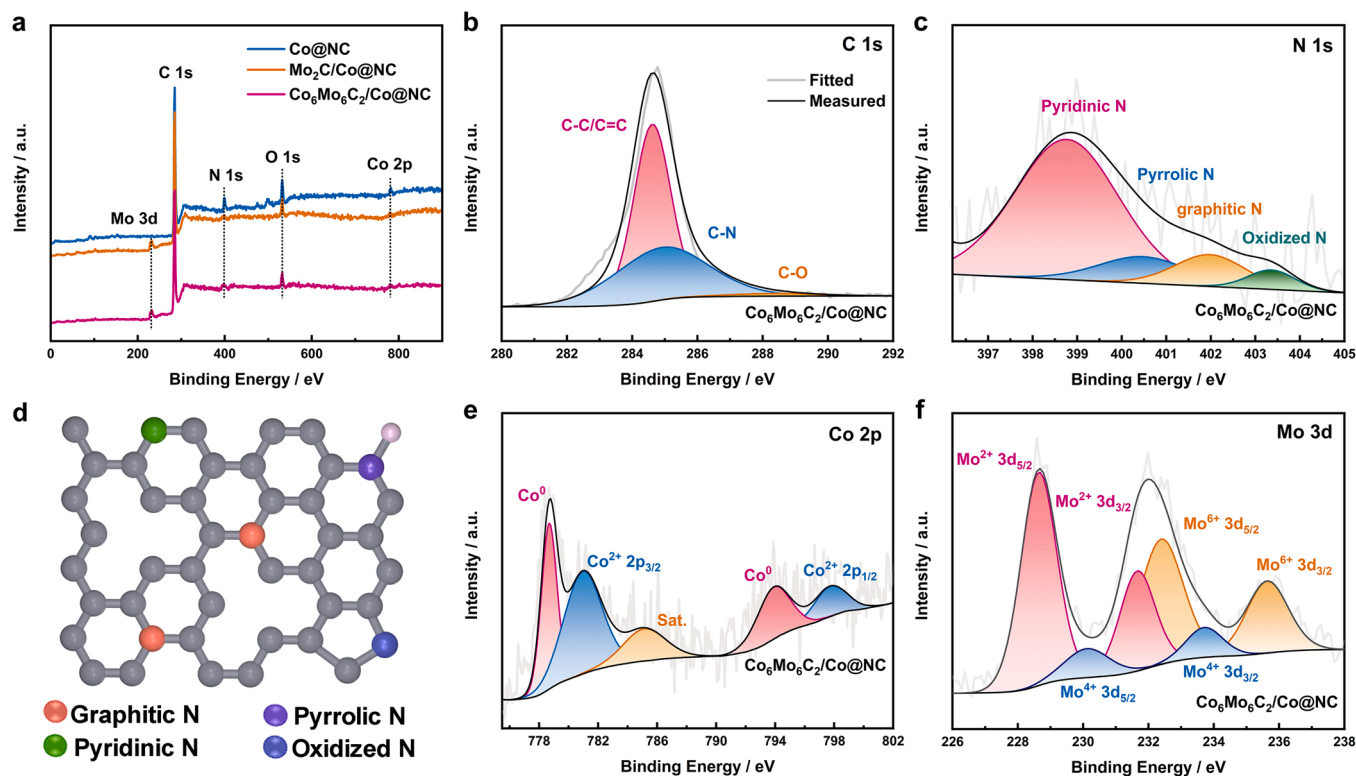


Fig. 4. (a) XPS survey spectra of as-prepared carbon-based Mott-Schottky catalysts. The related high-resolution XPS spectra of (b) C 1s, (c) N 1s, (d) schematic diagram of different N types, (e) Co 2p, and (f) Mo 3d of $\text{Co}_6\text{Mo}_6\text{C}_2/\text{Co@NC}$.

$\text{Co}_6\text{Mo}_6\text{C}_2/\text{Co@NC}$ is 58 mV dec^{-1} (Fig. 5c), which means the faster HER kinetics in $\text{Co}_6\text{Mo}_6\text{C}_2/\text{Co@NC}$. In alkaline HER, the H_2O adsorbed on the catalyst surface can undergo dissociation to generate OH^* and H^* , and then the active site was updated for subsequent H_2O re-adsorption. The area adjacent to the Mott-Schottky heterojunction contains electrophilic and nucleophilic regions that play a facilitating role in H_2O dissociation step, which ensure sufficient protons to promote HER [40]. It should be highlighted that $\text{Co}_6\text{Mo}_6\text{C}_2/\text{Co@NC}$ has dual active sites for H^* and OH^* . The $\text{Co}_6\text{Mo}_6\text{C}_2$ species, as effective H^* sites, have more suitable adsorption energy as compared with traditional Mo_2C because Mo_2C has unoccupied d -electron orbital, which makes it inclined to possess an excessive adsorption capacity in HER [41]. Co nanoparticles act as ideal OH^* active sites due to the desirable oxophilicity [25]. These distinct dual sites for H^* adsorption (on $\text{Co}_6\text{Mo}_6\text{C}_2$) and OH^* adsorption (on Co) can boost the water dissociation process and Volmer step by virtue of the synergy effect, thus resulting in good alkaline HER activity. The fitted EIS plots and parameters are shown in Fig. 5d and Table 1. $\text{Co}_6\text{Mo}_6\text{C}_2/\text{Co@NC}$ demonstrates the smallest R_{ct} ($10.76 \Omega \text{ cm}^2$), suggesting fast charge transfer between $\text{Co}_6\text{Mo}_6\text{C}_2/\text{Co@NC}$ and electrolyte interface, which is attributed to the high degree of graphitization of the 3D carbon matrix and abundant 1D tentacle-like CNTs, which facilitates electron transport.

Fig. 5e and Fig. S1b-d display the CV curves of Mott-Schottky catalysts and NF with the different scan rates. The computed value of C_{dl} for NF, Co@NC, $\text{Mo}_2\text{C}/\text{Co@NC}$, and $\text{Co}_6\text{Mo}_6\text{C}_2/\text{Co@NC}$ are 0.67, 1.03, 1.56, and 2.15 mF cm^{-2} respectively (Fig. 5f). The corresponding ECSA of $\text{Co}_6\text{Mo}_6\text{C}_2/\text{Co@NC}$ in Fig. S1e is 53.75 cm^2 , higher than other Mott-Schottky catalysts, suggesting that the $\text{Co}_6\text{Mo}_6\text{C}_2/\text{Co@NC}$ is prone to exposing more active sites owing to large BET surface area and hierarchical pore structures, as illustrated in BET analysis. The LSV curves was further normalized against ECSA. In Fig. S1f, the normalized η_{10} of $\text{Co}_6\text{Mo}_6\text{C}_2/\text{Co@NC}$ is 152 mV, which is lower than $\text{Mo}_2\text{C}/\text{Co@NC}$ (193 mV) and Co@NC (207 mV), indicating that $\text{Co}_6\text{Mo}_6\text{C}_2/\text{Co@NC}$ has a superior inherent catalytic activity. Due to the inherent superior

catalytic activity of noble metal-based catalysts, $\text{Co}_6\text{Mo}_6\text{C}_2/\text{Co@NC}$ is still not comparable. Fortunately, by virtue of good physical structure and chemical properties, the $\text{Co}_6\text{Mo}_6\text{C}_2/\text{Co@NC}$ catalyst exhibits satisfactory HER electrocatalytic activity in contrast to most reported carbon-based electrocatalysts (Table S3).

The durability of Mott-Schottky catalysts was assessed with LSV curves and CP methods in 1.0 M KOH electrolytes. Unlike Co@NC and $\text{Mo}_2\text{C}/\text{Co@NC}$, the LSV curve of $\text{Co}_6\text{Mo}_6\text{C}_2/\text{Co@NC}$ has only subtle changes after 1000 CV cycles, as shown in Fig. 5g, demonstrating its good long-term stability. For the CP test (Fig. 5h), the initial large drop in overpotential was due to the violent reaction triggered by the contact of the $\text{Co}_6\text{Mo}_6\text{C}_2/\text{Co@NC}$ with the electrolyte. But foremost, the $\text{Co}_6\text{Mo}_6\text{C}_2/\text{Co@NC}$ electrode maintains a relatively stable current density for 60 h (retention of 95.8 %), surpassing $\text{Mo}_2\text{C}/\text{Co@NC}$ (93.6 %) and Co@NC (87.0 %), proving the superior chemical and structural stability of $\text{Co}_6\text{Mo}_6\text{C}_2/\text{Co@NC}$ catalyst. After the stability test, the XRD, XPS, SEM, and TEM measurements were performed to further investigate the related HER mechanisms as well as the compositional and structural stability of the $\text{Co}_6\text{Mo}_6\text{C}_2/\text{Co@NC}$. The comparison of XRD (Fig. S2a) before and after durability test shows that the peaks of $\text{Co}_6\text{Mo}_6\text{C}_2/\text{Co@NC}$ become messy after the long-term work, which can be attributed to the strong interaction of the Co and $\text{Co}_6\text{Mo}_6\text{C}_2$ species with related reactants, resulting in nanoparticles aggregation [42,43]. TEM of $\text{Co}_6\text{Mo}_6\text{C}_2/\text{Co@NC}$ can further confirm this point, as shown in Fig. 5j-l. In addition, the XPS and SEM (Fig. S2b-e and Fig. 5i) after HER stability test in alkaline media suggest that there were no significant changes occurred in the composition, structure and morphology of $\text{Co}_6\text{Mo}_6\text{C}_2/\text{Co@NC}$. All these post-characterizations prove that Co and $\text{Co}_6\text{Mo}_6\text{C}_2$ are the ideal active sites for HER, and the $\text{Co}_6\text{Mo}_6\text{C}_2/\text{Co@NC}$ catalyst possesses good compositional and structural stability.

3.3. Electrochemical activity for IRR

Fig. 6 displays the electrochemical characterization and photovoltaic

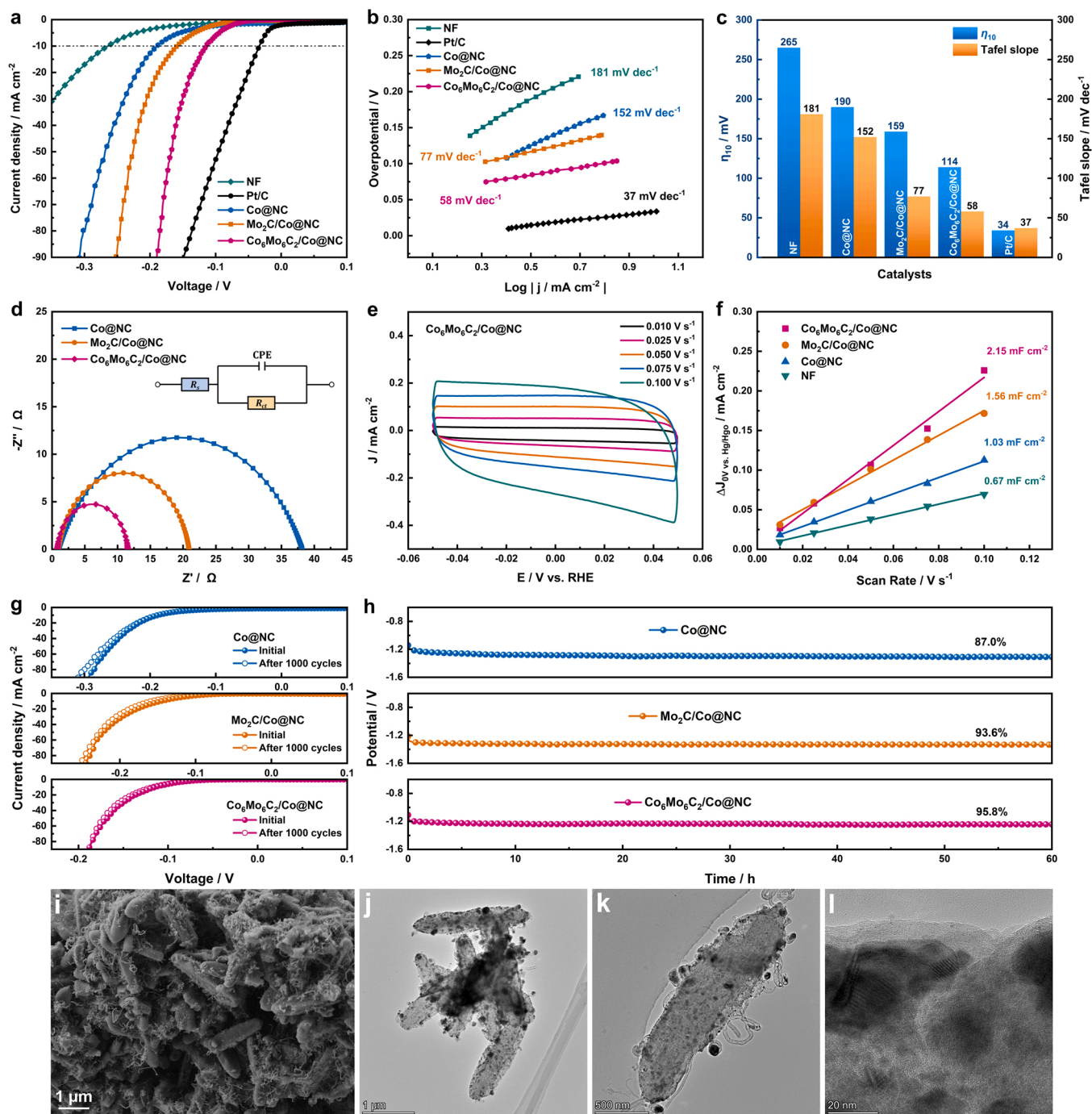


Fig. 5. (a) LSV curves, (b) Tafel plots, (c) η_{10} and Tafel slope values, and (d) Nyquist plots of as-obtained electrodes. (e) CV curves of Co₆Mo₆C₂/Co@NC with different scan rates. (f) C_{dl} results for as-obtained electrodes. (g) Initial and final LSV curves for 1000 CV cycles and (h) CP curves of as-obtained electrodes for HER. (i-l) SEM and TEM of Co₆Mo₆C₂/Co@NC after HER stability test.

performance of all Mott-Schottky catalysts and Pt. The specific data can be seen in Table 2. All the electrode catalysts in Fig. 6a exhibit two typical redox peaks, in which the redox peaks from the high to the low potential side represent $3I_2 + 2e^- \leftrightarrow 2I_3^-$ and $I_3^- + 2e^- \leftrightarrow 3I^-$ reactions, respectively [44,45]. In CV curve, peak-to-peak separation (ΔE_p) and peak current density (I_p) are key descriptors for evaluating catalytic performance [46,47]. The ΔE_p of Co₆Mo₆C₂/Co@NC is 0.50 V, which is smaller than Mo₂C/Co@NC (0.51 V) and Co@NC (0.52 V), indicating that the redox reaction proceeds smoothly on the Co₆Mo₆C₂/Co@NC electrode surface, which facilitates the rapid regeneration of the dye sensitizer. I_p values of carbon-based Mott-Schottky catalysts decrease in

the order of Co@NC (0.56 mA cm⁻²) < Mo₂C/Co@NC (1.15 mA cm⁻²) < Co₆Mo₆C₂/Co@NC (3.03 mA cm⁻²), proving that Co₆Mo₆C₂/Co@NC has excellent catalytic activity, even compared to Pt (0.96 mA cm⁻²). Furthermore, CV curves of Mott-Schottky catalysts and Pt with different rates are shown in Fig. S3a-d. The slope of $I_p-v^{1/2}$ curve is proportional to the active surface area. [16,48]. In Fig. S3e, Co₆Mo₆C₂/Co@NC ($S_{ox}=0.32$ and $S_{red}=0.37$) and Mo₂C/Co@NC ($S_{ox}=0.36$ and $S_{red}=0.40$) have similar slopes, higher than Co@NC ($S_{ox}=0.06$ and $S_{red}=0.07$) and Pt ($S_{ox}=0.14$ and $S_{red}=0.14$) electrodes. This result confirms that Co₆Mo₆C₂/Co@NC and Mo₂C/Co@NC have larger effective active surface area and thus good catalytic activity for IRR. EIS plots

Table 1

HER activity parameters for NF, Co@NC, Mo₂C/Co@NC, Co₆Mo₆C₂/Co@NC, and Pt/C^a.

Catalysts	η_{10} (mV vs. RHE)	Tafel slope (mV dec ⁻¹)	R_{ct} (Ω cm ²)	C_{dl} (mF cm ⁻²)	ECSA (cm ²)
NF	265	181	-	0.67	16.75
Co@NC	190	152	37.18	1.03	25.75
Mo ₂ C/Co@NC	159	77	19.94	1.56	39
Co ₆ Mo ₆ C ₂ /Co@NC	114	58	10.76	2.15	53.75
Pt/C	34	37	-	-	-

^a η_{10} : overpotential at current density of 10 mA cm⁻²; R_{ct} : charge transfer resistance.

are illustrated in Fig. 6b, in which the semicircle located at the high-frequency region means charge-transfer resistance (R_{ct}) value and the intercept on the X-axis represents series resistor (R_s) [49,50]. R_{ct} and R_s values (Table 2) of Co₆Mo₆C₂/Co@NC (0.56 and 11.69 Ω cm²) are lower than that of Co@NC (1.13 and 18.69 Ω cm²), Mo₂C/Co@NC (1.02 and 13.44 Ω cm²), and Pt (0.86 and 18.28 Ω cm²), indicating that Co₆Mo₆C₂/Co@NC has greater adhesion in the electrolyte/electrode film interface and superior electron transmission speed for I₃/I⁻. Fig. 6c reveals Tafel polarization curve of Co@NC, Mo₂C/Co@NC, and

Co₆Mo₆C₂/Co@NC. Exchange current density (J_0) and limiting diffusion current density (J_{lim}) correspond to intersection of the branch of linear extrapolation in the Tafel zone, and the branch and Y-axis intersection point, corresponding to Eq. 1 and Eq. 2 respectively.

$$J_0 = RT/nFR_{ct} \quad (1)$$

$$J_{lim} = 2nFCD/l \quad (2)$$

in which R is the gas constant, T is the thermodynamic temperature, n represents the electron number transferred in the reduction process, F represents the Faraday constant, C is the concentration of I₃, D is the I₃ ion diffusion coefficient, and l is the distance between the electrodes [51, 52]. Generally, a bigger slope yields a larger J_0 that implies a lower R_{ct} (Eq. 1), while larger J_{lim} value indicates that I₃ in the electrolyte has a greater diffusion speed (Eq. 2). Here, Co₆Mo₆C₂/Co@NC has the largest J_0 and J_{lim} , indicating the fast charge transfer and ion diffusion between the Co₆Mo₆C₂/Co@NC electrode and electrolyte, which are beneficial to the IRR. The acquired parameters value including I_p , ΔE_p , and R_{ct} suggest that the Co₆Mo₆C₂/Co@NC catalyst possesses satisfactory conductivity and IRR activity, which can be mainly attributed to its unique morphology, that is, 1D carbon nanotubes and 3D carbon matrix. Concretely, 1D carbon nanotubes and 3D N-modified carbon matrix possesses the high graphitization degree and porous structure that not

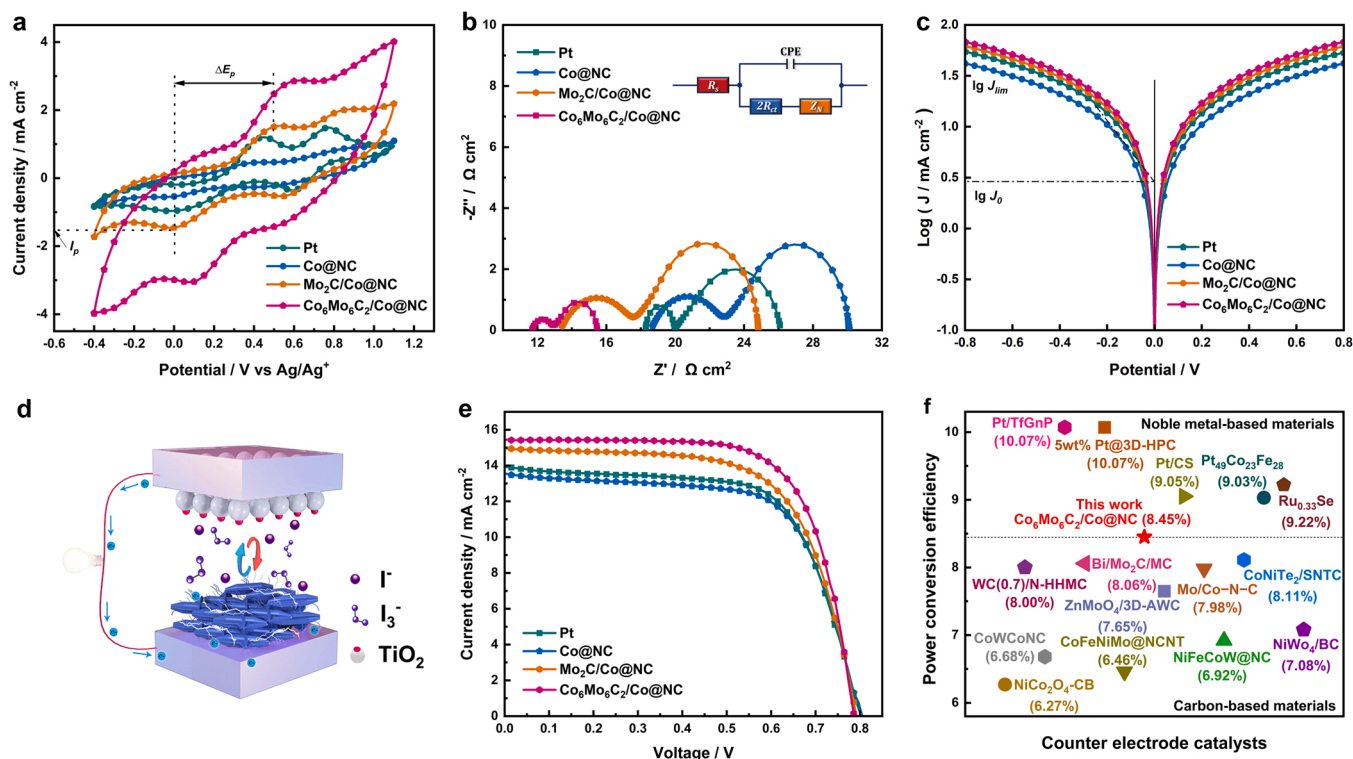


Fig. 6. (a) CV curves, (b) EIS plots (insert: equivalent circuit), and (c) Tafel polarization plots of as-prepared carbon-based Mott-Schottky catalysts. (d) Assembling schematic of photovoltaic device. (e) J - V curves for the best solar cells. (f) PCE of solar cells with different counter electrodes (Detailed photovoltaic parameters can be found in Table S5).

Table 2

Photovoltaic and electrochemical parameters of Co@NC, Mo₂C/Co@NC, Co₆Mo₆C₂/Co@NC, and Pt.

Catalysts	J_{sc} (mA cm ⁻²)	V_{oc} (V)	PCE (%)	FF	ΔE_p (V)	I_p (mA cm ⁻²)	R_s (Ω cm ²)	R_{ct} (Ω cm ²)	J_0 (mA cm ⁻²)
Co@NC	13.59	0.80	7.21	0.66	0.52	-0.56	18.69	1.13	2.51
Mo ₂ C/Co@NC	14.94	0.79	7.78	0.66	0.51	-1.15	13.44	1.02	3.63
Co ₆ Mo ₆ C ₂ /Co@NC	15.25	0.79	8.45	0.71	0.50	-3.03	11.69	0.56	4.37
Pt	13.99	0.80	7.38	0.66	0.50	-0.96	18.28	0.86	3.47

J_{sc} : short-circuit current density; V_{oc} : open-circuit voltage; PCE: power conversion efficiency; FF: fill factor; ΔE_p : peak-to-peak separation; I_p : peak current density; R_s : series resistor; R_{ct} : charge-transfer resistance; J_0 : exchange current density.

only ensure fast electron transport but also guarantee more adequate contact of I_3^- with active sites [53,54].

Fig. 6d shows a solar cell with a sandwich structure (photoanode/electrolyte/counter electrode) for photovoltaic testing. The J - V curves of as-prepared Mott-Schottky catalysts are shown in Fig. 6e. The solar cell fabricated with $Co_6Mo_6C_2/Co@NC$ counter electrode delivers a PCE of 8.45 % (J_{sc} = 15.25 mA cm⁻², FF=0.71, and V_{oc} =0.79 V), obviously greater than that of solar cell with $Co@NC$ (7.21 %), $Mo_2C/Co@NC$ (7.78 %), and Pt (7.38 %) counter electrodes. (The error analysis of photovoltaic data is shown in Table S4.) Notably, the $Co_6Mo_6C_2/Co@NC$ electrode catalyst with good conductivity and desirable catalytic activity can ensure the effective reduction of I_3^- to I^- and thus the fast dye regeneration on TiO_2 , leading to a higher J_{sc} of $Co_6Mo_6C_2/Co@NC$ based solar cell than the others [55,56]. Comparing with noble metal-based catalysts, $Co_6Mo_6C_2/Co@NC$ remains inferior, but still outperforms most reported carbon-based catalysts (Fig. 6f and Table S5).

To evaluate the durability of Mott-Schottky catalysts, CV multicycle scanning and photo response tests were performed. Better overlap can be observed in Fig. 7a-d after 50 CV cycles, suggesting that all Mott-Schottky catalysts have favorable chemical stability. Furthermore, the relationship between the peak current and cycle times of the as-prepared materials is displayed in Fig. 7e-h. The $Co_6Mo_6C_2/Co@NC$ has good oxidation and reduction current density durability, mainly because of the high degree of graphitization of the CNTs. When illuminated, the assembled cells respond quickly under simulated light, indicating an excellent photo-response capability of the catalyst materials (Fig. 7i). After continuous switch measurements, the photocurrent density of

$Co_6Mo_6C_2/Co@NC$ is 96.0 % of the initial value, which is better than of others in Fig. 7j, proving the greater stability of $Co_6Mo_6C_2/Co@NC$ counter electrode in the IRR. The outstanding IRR stability of $Co_6Mo_6C_2/Co@NC$ is ascribed to the 1D carbon nanotubes and 3D carbon matrix with high graphitization degree, which act as armor, encasing the metallic nanoparticles in a carbon matrix to protect them from rapid corrosion by the electrolyte.

4. Understanding boosting electron transfer behavior in dual Mott-Schottky heterojunctions catalyst

The determination of the Fermi energy levels in $Co@NC$, $Mo_2C/Co@NC$, and $Co_6Mo_6C_2/Co@NC$ was performed using ultraviolet photoelectron spectroscopy (UPS). Generally, the contact potential difference between the metal and NC with different W_f drives the electron transport at the heterojunction interface. The electrons tend to escape from the matrix with a small W_f to the other side with a large W_f until their Fermi energy levels become balanced based on the Mott-Schottky effects [57]. The W_f value was decided by the equation $W_f = 21.21 \text{ eV} - (E_{cutoff} - E_f)$, where the 21.21 eV represents the photon energy, E_{cutoff} and E_f denote the low energy cut-off edge and the Fermi level (More details in Fig. S4). In Fig. 8a, the W_f values of all as-prepared Mott-Schottky catalysts rank in the following order: $Co@NC$ (3.46 eV) < $Mo_2C/Co@NC$ (3.76 eV) < $Co_6Mo_6C_2/Co@NC$ (4.01 eV). The progressively enlarged W_f indicates an increase in Fermi-level difference (ΔW_f) between metallic substances and NC supports. Therefore, the $Co_6Mo_6C_2/NC$ heterojunction exhibits the greatest contact potential difference at the Fermi level compared to $Co@NC$ and Mo_2C/NC , which

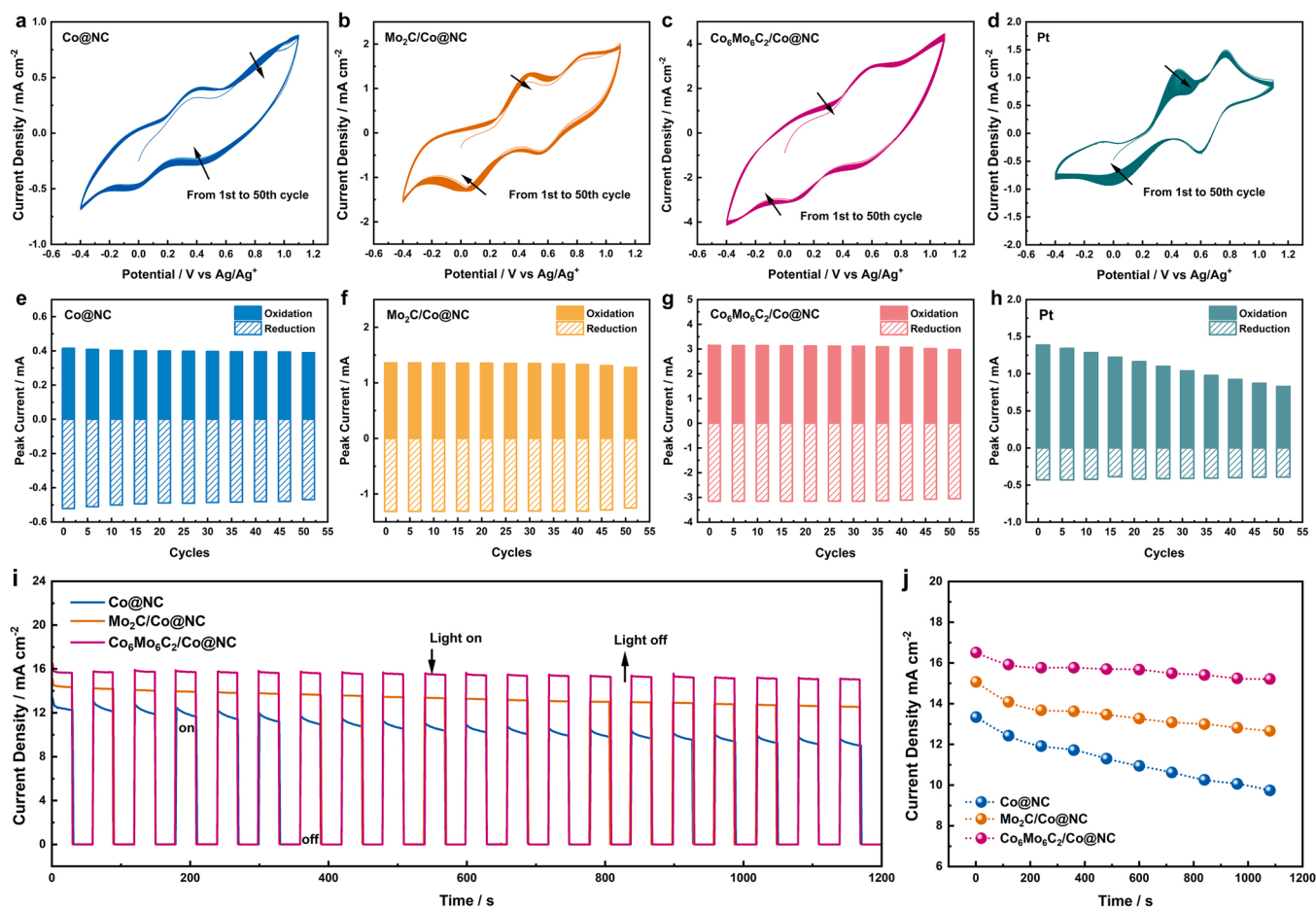


Fig. 7. Stability evaluation for IRR. 50 cycles CV curves of (a) $Co@NC$, (b) $Mo_2C/Co@NC$, (c) $Co_6Mo_6C_2/Co@NC$, and (d) Pt. The change of oxidation and reduction peak current density under various CV cycles of (e) $Co@NC$, (f) $Mo_2C/Co@NC$, (g) $Co_6Mo_6C_2/Co@NC$, and (h) Pt. (i) Photoresponse test and (j) corresponding stability of current density for $Co@NC$, $Mo_2C/Co@NC$, and $Co_6Mo_6C_2/Co@NC$.

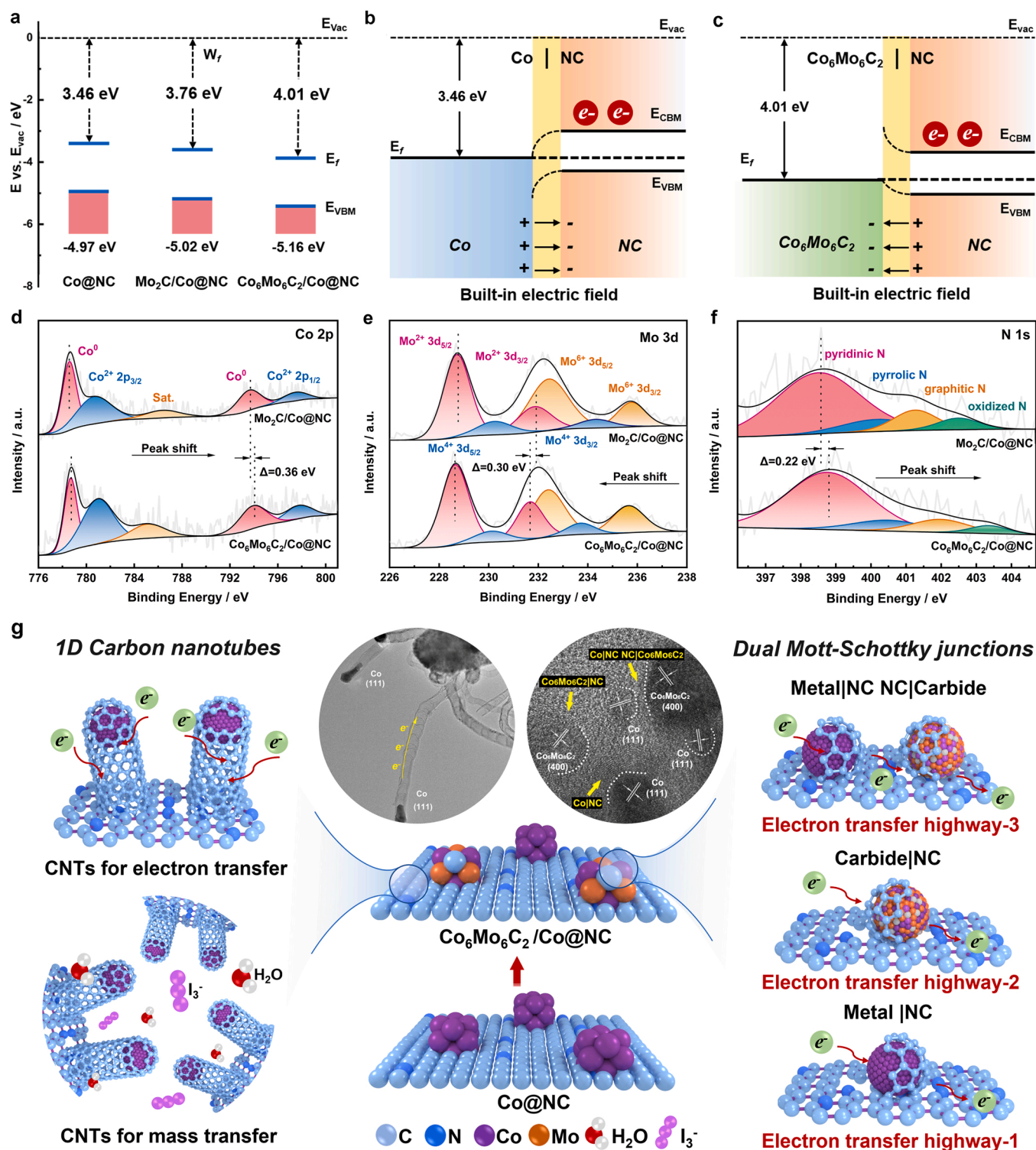


Fig. 8. (a) Energy-band plot of Co@NC, Mo₂C/Co@NC and Co₆Mo₆C₂/Co@NC. Schematic illustration of the dual Mott-Schottky heterojunctions: (b) Co|NC and (c) Co₆Mo₆C₂|NC for Co₆Mo₆C₂/Co@NC sample. XPS for (d) Co 2p, (e) Mo 3d, and (f) N 1s of Mo₂C/Co@NC and Co₆Mo₆C₂/Co@NC. (g) The schematic illustration of 1D/3D-structured dual Mott-Schottky heterojunctions (Co|NC and Co₆Mo₆C₂|NC) in Co₆Mo₆C₂/Co@NC (electron transfer highway-1: Co→NC; highway-2: NC→Co₆Mo₆C₂; highway-3: Co→NC→Co₆Mo₆C₂).

can induce electron transfer more efficiently [58,59].

To understand the electron transfer behavior of the dual Mott-Schottky heterojunctions catalyst, the electron transfer direction is clearly illustrated in Fig. 8b-c. At the Co|NC interface, electron flow occurs from Co to NC, whereas at the Co₆Mo₆C₂|NC interface, electrons flow from NC to Co₆Mo₆C₂. This electron transfer achieves an equal

Fermi energy level, which can bend the energy bands and trigger a built-in electric field at Mott-Schottky interfaces (yellow region). Similarly, the dual Mott-Schottky heterojunctions in Mo₂C/Co@NC (Co|NC and Mo₂C|NC) have a similar electron transmission path or direction as Co₆Mo₆C₂/Co@NC (Co₆Mo₆C₂|NC and Co|NC), where NC functions as both the electron donor and receiver. The intensity of the built-in

electric field is closely related to the ΔW_f -induced interfacial driving force, and a more vigorous built-in electric field can effectively accelerate the electron transfer [23]. Hence, compared with $\text{Mo}_2\text{C}/\text{NC}$, $\text{Co}_6\text{Mo}_6\text{C}_2/\text{NC}$ accompanied by Co/NC have established more efficient electron transfer highways to increase the electron transfer capability of $\text{Co}_6\text{Mo}_6\text{C}_2/\text{Co@NC}$, thereby achieving outstanding catalytic activity towards IRR and HER.

The electronic structure of Co can be indirectly modulated by modulating ΔW_f (from $\text{Mo}_2\text{C}/\text{NC}$ to $\text{Co}_6\text{Mo}_6\text{C}_2/\text{NC}$). In Fig. 8d, the Co^0 and Co^{2+} binding energies shift to higher binding energies by ca. 0.36 eV after Mo_2C is converted to $\text{Co}_6\text{Mo}_6\text{C}_2$, indicating that metallic Co is in a state of electron deficiency, which favors the adsorption or desorption of intermediates in HER [60,61]. In contrast, the Mo peak of $\text{Co}_6\text{Mo}_6\text{C}_2/\text{Co@NC}$ shifts about 0.30 eV to a lower binding energy than that of $\text{Mo}_2\text{C}/\text{Co@NC}$, suggesting the formation of electron-rich $\text{Co}_6\text{Mo}_6\text{C}_2$ species (Fig. 8e). The electron-rich $\text{Co}_6\text{Mo}_6\text{C}_2$ possesses a more suitable $\Delta G_{(\text{H}^*)}$ than Mo_2C , because the latter has a large-density of unoccupied *d*-orbitals that restrict HER kinetics [62,63]. In Fig. 8f, the binding energy of N 1s in $\text{Co}_6\text{Mo}_6\text{C}_2/\text{Co@NC}$ has a more positive shift by 0.22 eV than that of the $\text{Mo}_2\text{C}/\text{Co@NC}$, proving that the N species are endowed with lower electron density, which confirmed that electrons can be transmitted from NC to $\text{Co}_6\text{Mo}_6\text{C}_2$ via heterojunction interfaces. Overly, the increased ΔW_f between metal carbide/NC interfaces indirectly regulates the electronic structure of Co without changing its composition, as the XPS confirmed.

To understand the electron transport behavior more readily, Fig. 8g presents a schematic diagram of as-obtained Mott-Schottky carbon-based catalysts. In contrast to Co@NC , $\text{Co}_6\text{Mo}_6\text{C}_2/\text{Co@NC}$ contains abundant 1D CNTs and 3D carbon matrix. The dense 1D CNTs at the surface of $\text{Co}_6\text{Mo}_6\text{C}_2/\text{Co@NC}$ are crucial for promoting the catalytic process, as vividly displayed in the left part of Fig. 8g. On the one hand, the structure of Co nanoparticles wrapped in 1D CNTs is conducive for regulating the local electron environment to boost electron transfer (illustrated in the left TEM images in the middle part of Fig. 8g). On the other hand, the hollow channel structure of 1D CNTs could facilitate the mass transfer. The advantages of the 3D carbon matrix are as follows: i) 3D N-modified carbon matrix with uniform morphology and unique pore architecture can adequately contact the electrolyte and reaction site to accelerate the reaction process, as demonstrated by BET and contact angle tests. ii) 3D N-modified carbon matrix with high graphitization (as confirmed by Raman) can protect Co and $\text{Co}_6\text{Mo}_6\text{C}_2$ nanoparticles from electrolyte corrosion. The dual Mott-Schottky interfaces consisting of Co/NC and $\text{Co}_6\text{Mo}_6\text{C}_2/\text{NC}$, as shown in the right TEM image in the middle section of Fig. 8g, can trigger built-in electric fields that drive electron transport, thus establishing multiple electronic transfer highways. The Co@NC with single Mott-Schottky heterojunction catalyst has only one electron transfer highway (electron transfer highway-1: $\text{Co} \rightarrow \text{NC}$). In contrast, the constructed dual Mott-Schottky heterojunctions in $\text{Mo}_2\text{C}/\text{Co@NC}$ and $\text{Co}_6\text{Mo}_6\text{C}_2/\text{Co@NC}$ catalysts exhibit three potential electron transfer highways ($\text{Co} \rightarrow \text{NC}$, $\text{NC} \rightarrow \text{Co}_6\text{Mo}_6\text{C}_2$ or Mo_2C , and $\text{Co} \rightarrow \text{NC} \rightarrow \text{Co}_6\text{Mo}_6\text{C}_2$ or Mo_2C), as shown in the right part of Fig. 8g. With the aid of these electron transfer highways, the electrons can be transmitted more smoothly in the carbon matrix, and the electronic structure and density of the active sites of $\text{Co}_6\text{Mo}_6\text{C}_2/\text{Co@NC}$ could be effectively regulated. Briefly, constructing dual Mott-Schottky heterojunctions (Co/NC and $\text{Co}_6\text{Mo}_6\text{C}_2/\text{NC}$) with large ΔW_f in 1D/3D trepan-like $\text{Co}_6\text{Mo}_6\text{C}_2/\text{Co@NC}$ can trigger robust built-in electric fields to drive electron transport and regulate the electronic structure of the active sites for efficient IRR and HER.

5. Conclusion

In summary, a novel 1D/3D trepan-like porous N-doped carbon-encapsulated Co and $\text{Co}_6\text{Mo}_6\text{C}_2$ nanoparticles with in-situ grown tentacle-like CNTs ($\text{Co}_6\text{Mo}_6\text{C}_2/\text{Co@NC}$) was successfully developed as a dual Mott-Schottky heterojunctions catalyst. The resulting $\text{Co}_6\text{Mo}_6\text{C}_2/$

Co@NC exhibited a larger specific surface area ($310 \text{ m}^2/\text{g}$), high graphitization degree, and greater W_f (4.01 eV). The enlarged ΔW_f of $\text{Co}_6\text{Mo}_6\text{C}_2/\text{Co@NC}$ not only simultaneously optimized the electronic structure and electron density of the active sites adjacent to the dual Mott-Schottky interfaces, but also triggered a more robust built-in electric field to establish more electron transfer highways to boost electron transfer. As expected, $\text{Co}_6\text{Mo}_6\text{C}_2/\text{Co@NC}$ exhibited superior catalytic performance and an ideal overpotential ($\eta_{10} = 114 \text{ mV}$) and a small Tafel slope (58 mV dec^{-1}) in alkaline HER. The solar cell fabricated with $\text{Co}_6\text{Mo}_6\text{C}_2/\text{Co@NC}$ counter electrode achieved a satisfactory power conversion efficiency of 8.45 %. This work provides several insights into the dual Mott-Schottky heterojunctions for boosting electron transfer and regulating the electronic structures of active sites.

CRediT authorship contribution statement

Dan Qiao: Investigation, Formal analysis, Data curation, Visualization, Writing - original draft. **Sining Yun:** Conceptualization, Supervision, Methodology, Resources, Visualization, Funding acquisition, Project administration, Writing - review & editing. **Menglong Sun:** Formal analysis, Methodology, Investigation. **Jiaoe Dang:** Methodology, Investigation. **Yongwei Zhang:** Methodology, Investigation. **Shuangxi Yuan:** Methodology, Investigation. **Guangping Yang:** Methodology, Investigation. **Tianxiang Yang:** Methodology. **Zan Gao:** Methodology. **Zhiguo Wang:** Methodology.

Declaration of Competing Interest

The authors declare that they have no known competing financial interests or personal relationships that could have appeared to influence the work reported in this paper.

Data Availability

Data will be made available on request.

Acknowledgments

Financial support from NSFC (51672208), Key Program for International S&T Cooperation Projects of Shaanxi Province (2019KWZ-03), Key Program for Nature Science Foundation of Shaanxi Province (2019JZ-20), and Key Science and Technology Innovation Team of Shaanxi Province (2022TD-34) is greatly acknowledged.

Appendix A. Supporting information

Supplementary data associated with this article can be found in the online version at doi:10.1016/j.apcatb.2023.122830.

References

- [1] S. Chu, A. Majumdar, Opportunities and challenges for a sustainable energy future, *Nature* 488 (2012) 294–303, <https://doi.org/10.1038/nature11475>.
- [2] S. Yun, Y. Zhang, Q. Xu, J. Liu, Y. Qin, Recent advance in new-generation integrated devices for energy harvesting and storage, *Nano Energy* 60 (2019) 600–619, <https://doi.org/10.1016/j.nanoen.2019.03.074>.
- [3] X. Wang, B. Zhao, W. Kan, Y. Xie, K. Pan, Review on low-cost counter electrode materials for dye-sensitized solar cells: effective strategy to improve photovoltaic performance, *Adv. Mater. Interfaces* 9 (2022), 2101229, <https://doi.org/10.1002/admi.202101229>.
- [4] C. Lv, T. Zhang, X. Wang, H. Pan, Z. Xie, H. Lu, K. Pan, Y. Xie, Enhancement of the triiodide reduction reaction by doping molybdenum in NiSe hierarchical microspheres: a theoretical and experimental study, *Inorg. Chem. Front.* 10 (2023) 460–467, <https://doi.org/10.1039/d2qi02029g>.
- [5] L. Sun, T. Zhang, Y. Liu, J. Wang, W. Zong, Y. Cao, X. Wang, Hierarchical NiSe microspheres as high-efficiency counter electrode catalysts for triiodide reduction reaction, *Sol. Energy* 225 (2021) 486–493, <https://doi.org/10.1016/j.solener.2021.07.058>.
- [6] Y. Cao, P. Yu, L. Wang, X. Wang, L. Li, M. Yu, C. Sun, Z. Liu, B. Zhao, Edge-active enriched MoS_2 porous nanosheets as efficient Pt-free catalysts toward the triiodide

- reduction reaction, *ACS Appl. Electron. Mater.* 5 (2023) 429–439, <https://doi.org/10.1021/acsaem.2c01445>.
- [7] S. Yun, A. Hagfeldt, T. Ma, Pt-free counter electrode for dye-sensitized solar cells with high efficiency, *Adv. Mater.* 26 (2014) 6210–6237, <https://doi.org/10.1002/adma.201402056>.
 - [8] Y. Qu, B. Chen, Z. Li, X. Duan, L. Wang, Y. Lin, T. Yuan, F. Zhou, Y. Hu, Z. Yang, C. Zhao, J. Wang, C. Zhao, Y. Hu, G. Wu, Q. Zhang, Q. Xu, B. Liu, P. Gao, R. You, W. Huang, L. Zheng, L. Gu, Y. Wu, Y. Li, Thermal emitting strategy to synthesize atomically dispersed Pt metal sites from bulk Pt metal, *J. Am. Chem. Soc.* 141 (2019) 4505–4509, <https://doi.org/10.1021/jacs.8b09834>.
 - [9] Y. Zhu, H. Guo, H. Zheng, Y.-n Lin, C. Gao, Q. Han, M. Wu, Choose a reasonable counter electrode catalyst toward a fixed redox couple in dye-sensitized solar cells, *Nano Energy* 21 (2016) 1–18, <https://doi.org/10.1016/j.nanoen.2016.01.001>.
 - [10] S. Emin, C. Altinkaya, A. Semerci, H. Okuyucu, A. Yildiz, P. Stefanov, Tungsten carbide electrocatalysts prepared from metallic tungsten nanoparticles for efficient hydrogen evolution, *Appl. Catal. B: Environ.* 236 (2018) 147–153, <https://doi.org/10.1016/j.apcatb.2018.05.026>.
 - [11] H. Lin, N. Liu, Z. Shi, Y. Guo, Y. Tang, Q. Gao, Cobalt-doping in molybdenum-carbide nanowires toward efficient electrocatalytic hydrogen evolution, *Adv. Funct. Mater.* 26 (2016) 5590–5598, <https://doi.org/10.1002/adfm.201600915>.
 - [12] A. Radwan, H. Jin, D. He, S. Mu, Design engineering, synthesis protocols, and energy applications of MOF-derived electrocatalysts, *Nanomicro Lett.* 13 (2021) 132, <https://doi.org/10.1007/s40820-021-00656-w>.
 - [13] C. Yang, K. Shen, R. Zhao, H. Xiang, J. Wu, W. Zhong, Q. Zhang, X. Li, N. Yang, Balance effect: a universal strategy for transition metal carbides to enhance hydrogen evolution, *Adv. Funct. Mater.* 32 (2022), 2108167, <https://doi.org/10.1002/adfm.202108167>.
 - [14] T. Zhang, C. Lv, X. Wang, S. Wang, Y. Xie, M. Yu, C. Sun, K. Pan, Surface active-site engineering in NiCoSe₂/nitrogen-doped carbon dodecahedrons for efficient triiodide reduction in photovoltaics, *Appl. Surf. Sci.* 610 (2023), 155483, <https://doi.org/10.1016/j.apsusc.2022.155483>.
 - [15] Z. Liu, W. Xin, W. Xie, X. Wang, N. Li, Z. Yuan, Y. Li, J. Wang, Integration of hierarchical tin Sulfide@Sulfur-Doped carbon porous composites with enhanced performance for triiodide reduction, *Dyes Pigm.* 204 (2022), 110458, <https://doi.org/10.1016/j.dyepig.2022.110458>.
 - [16] T. Song, Z. Zhang, B. Zhao, L. Wang, W. Kan, L. Sun, X. Wang, Boosting catalytic performance of hierarchical Co/Co_{0.85}Se microspheres via Mott-Schottky effect toward triiodide reduction and alkaline hydrogen evolution, *J. Alloy Compd.* 918 (2022), 165608, <https://doi.org/10.1016/j.jallcom.2022.165608>.
 - [17] X.H. Li, M. Antonietti, Metal nanoparticles at mesoporous N-doped carbons and carbon nitrides: functional Mott-Schottky heterojunctions for catalysis, *Chem. Soc. Rev.* 42 (2013) 6593–6604, <https://doi.org/10.1039/c3cs60067j>.
 - [18] Z. Li, M. Hu, P. Wang, J. Liu, J. Yao, C. Li, Heterojunction catalyst in electrocatalytic water splitting, *Coord. Chem. Rev.* 439 (2021), 213953, <https://doi.org/10.1016/j.ccr.2021.213953>.
 - [19] M. Sun, S. Yun, J. Dang, Y. Zhang, Z. Liu, D. Qiao, 1D/3D rambutan-like Mott-Schottky porous carbon polyhedrons for efficient tri-iodide reduction and hydrogen evolution reaction, *Chem. Eng. J.* 458 (2023), 141301, <https://doi.org/10.1016/j.cej.2023.141301>.
 - [20] Q. Zhang, F. Luo, X. Long, X. Yu, K. Qu, Z. Yang, N. P. doped carbon nanotubes confined WN-Ni Mott-Schottky heterogeneous electrocatalyst for water splitting and rechargeable zinc-air batteries, *Appl. Catal. B: Environ.* 298 (2021), 120511, <https://doi.org/10.1016/j.apcatb.2021.120511>.
 - [21] Y. Dong, Y. Liu, Y. Hu, K. Ma, H. Jiang, C. Li, Boosting reaction kinetics and reversibility in Mott-Schottky VS₂/MoS₂ heterojunctions for enhanced lithium storage, *Sci. Bull.* 65 (2020) 1470–1478, <https://doi.org/10.1016/j.scib.2020.05.007>.
 - [22] L. Peng, L. Su, X. Yu, R. Wang, X. Cui, H. Tian, S. Cao, B.Y. Xia, J. Shi, Electron redistribution of ruthenium-tungsten oxides Mott-Schottky heterojunction for enhanced hydrogen evolution, *Appl. Catal. B: Environ.* 308 (2022), 121229, <https://doi.org/10.1016/j.apcatb.2022.121229>.
 - [23] L. Zhai, X. She, L. Zhuang, Y. Li, R. Ding, X. Guo, Y. Zhang, Y. Zhu, K. Xu, H.J. Fan, S.P. Lau, Modulating built-in electric field via variable oxygen affinity for robust hydrogen evolution reaction in neutral media, *Angew. Chem. Int. Ed.* 61 (2022), e202116057, <https://doi.org/10.1002/anie.202116057>.
 - [24] S. Ni, H. Qu, Z. Xu, X. Zhu, H. Xing, L. Wang, J. Yu, H. Liu, C. Chen, L. Yang, Interfacial engineering of the NiSe₂/FeSe₂ p-p heterojunction for promoting oxygen evolution reaction and electrocatalytic urea oxidation, *Appl. Catal. B: Environ.* 299 (2021), 120638, <https://doi.org/10.1016/j.apcatb.2021.120638>.
 - [25] K.P. Kepp, A quantitative scale of oxophilicity and thiophilicity, *Inorg. Chem.* 55 (2016) 9461–9470, <https://doi.org/10.1021/acs.inorgchem.6b01702>.
 - [26] C. Yang, S. Yun, J. Shi, M. Sun, N. Zafar, A. Arshad, Y. Zhang, L. Zhang, Tailoring the supercapacitive behaviors of Co/Zn-ZIF derived nanoporous carbon via incorporating transition metal species: a hybrid experimental-computational exploration, *Chem. Eng. J.* 419 (2021), 129636, <https://doi.org/10.1016/j.cej.2021.129636>.
 - [27] C. Wang, S. Yun, H. Xu, Z. Wang, F. Han, Y. Zhang, Y. Si, M. Sun, Dual functional application of pomelo peel-derived bio-based carbon with controllable morphologies: An efficient catalyst for triiodide reduction and accelerant for anaerobic digestion, *Ceram. Int.* 46 (2020) 3292–3303, <https://doi.org/10.1016/j.ceramint.2019.10.035>.
 - [28] J. Wang, F. Ciucci, In-situ synthesis of bimetallic phosphide with carbon tubes as an active electrocatalyst for oxygen evolution reaction, *Appl. Catal. B: Environ.* 254 (2019) 292–299, <https://doi.org/10.1016/j.apcatb.2019.05.009>.
 - [29] X. Wang, S. Yun, W. Fang, C. Zhang, X. Liang, Z. Lei, Z. Liu, Layer-stacking activated carbon derived from sunflower stalk as electrode materials for high-performance supercapacitors, *ACS Sustain. Chem. Eng.* 6 (2018) 11397–11407, <https://doi.org/10.1021/acssuschemeng.8b01334>.
 - [30] Z. Sun, Y. Wang, L. Zhang, H. Wu, Y. Jin, Y. Li, Y. Shi, T. Zhu, H. Mao, J. Liu, C. Xiao, S. Ding, Simultaneously realizing rapid electron transfer and mass transport in jellyfish-like mott-schottky nanoreactors for oxygen reduction reaction, *Adv. Funct. Mater.* 30 (2020), 1910482, <https://doi.org/10.1002/adfm.201910482>.
 - [31] X. Zhao, P. Pachfule, S. Li, J.R.J. Simke, J. Schmidt, A. Thomas, Bifunctional electrocatalysts for overall water splitting from an iron/nickel-based bimetallic metal-organic framework/dicyandiamide composite, *Angew. Chem. Int. Ed.* 57 (2018) 8921–8926, <https://doi.org/10.1002/anie.201803136>.
 - [32] X. Zhu, H. Qiu, P. Chen, G. Chen, W. Min, Anemone-shaped ZIF-67@CNTs as effective electromagnetic absorbent covered the whole X-band, *Carbon* 173 (2021) 1–10, <https://doi.org/10.1016/j.carbon.2020.10.055>.
 - [33] F. Xing, H. Yu, C. Cheng, Q. Liu, L. Lai, S. Xia, C. Huang, Interfacial microenvironment-regulated cascade charge transport in Co₉Mo₆C₂-MoO₂-CoNC@ZnIn₂S₄ photocatalyst for efficient hydrogen evolution, *Chem. Eng. J.* 450 (2022), 138130, <https://doi.org/10.1016/j.cej.2022.138130>.
 - [34] H. Li, M. Hu, L. Zhang, L. Huo, P. Jing, B. Liu, R. Gao, J. Zhang, B. Liu, Hybridization of bimetallic molybdenum-tungsten carbide with nitrogen-doped carbon: a rational design of super active porous composite nanowires with tailored electrocatalytic structure for boosting hydrogen evolution catalysis, *Adv. Funct. Mater.* 30 (2020), 2003198, <https://doi.org/10.1002/adfm.202003198>.
 - [35] J. Ge, L. Fan, J. Wang, Q. Zhang, Z. Liu, E. Zhang, Q. Liu, X. Yu, B. Lu, MoSe₂/N-doped carbon as anodes for potassium-ion batteries, *Adv. Energy Mater.* 8 (2018), 1801477, <https://doi.org/10.1002/aenm.201801477>.
 - [36] G. Zhou, G. Liu, X. Liu, Q. Yu, H. Mao, Z. Xiao, L. Wang, 1D/3D heterogeneous assembling body as trifunctional electrocatalysts enabling zinc-air battery and self-powered overall water splitting, *Adv. Funct. Mater.* 32 (2022), 2107608, <https://doi.org/10.1002/adfm.202107608>.
 - [37] K. Fu, Y. Wang, L. Mao, X. Yang, J. Jin, S. Yang, G. Li, Strongly coupled Co, N doped carbon nanotubes/graphene-like carbon nanosheets as efficient oxygen reduction electrocatalysts for primary Zinc-air battery, *Chem. Eng. J.* 351 (2018) 94–102, <https://doi.org/10.1016/j.cej.2018.06.059>.
 - [38] Z. Zhou, Z. Yuan, S. Li, H. Li, J. Chen, Y. Wang, Q. Huang, C. Wang, H.E. Karahan, G. Henkelman, X. Liao, L. Wei, Y. Chen, Big to small: ultrafine Mo₂C particles derived from giant polyoxomolybdate clusters for hydrogen evolution reaction, *Small* 15 (2019), e1900358, <https://doi.org/10.1002/smll.201900358>.
 - [39] Y. Zheng, J. Dong, C. Huang, L. Xia, Q. Wu, Q. Xu, W. Yao, Co-doped Mo-Mo₂C cocatalyst for enhanced g-C₃N₄ photocatalytic H₂ evolution, *Appl. Catal. B: Environ.* 260 (2020), 118220, <https://doi.org/10.1016/j.apcatb.2019.118220>.
 - [40] Y. Zhang, Y. Qiu, Z. Ma, Y. Wang, Y. Zhang, Y. Ying, Y. Jiang, Y. Zhu, S. Liu, Core-corona Co/CoP clusters strung on carbon nanotubes as a Schottky catalyst for glucose oxidation assisted H₂ production, *J. Mater. Chem. A* 9 (2021) 10893–10908, <https://doi.org/10.1039/D0TA11850H>.
 - [41] S. Yuan, M. Xia, Z. Liu, K. Wang, L. Xiang, G. Huang, J. Zhang, N. Li, Dual synergistic effects between Co and Mo₂C in Co/Mo₂C heterostructure for electrocatalytic overall water splitting, *Chem. Eng. J.* 430 (2022), 132697, <https://doi.org/10.1016/j.cej.2021.132697>.
 - [42] N. Yao, P. Li, Z. Zhou, R. Meng, G. Cheng, W. Luo, Nitrogen engineering on 3D dandelion-flower-like CoS₂ for high-performance overall water splitting, *Small* 15 (2019), e1901993, <https://doi.org/10.1002/smll.201901993>.
 - [43] B. You, N. Jiang, M. Sheng, M.W. Bhusan, Y. Sun, Hierarchically porous urchin-like Ni₂P superstructures supported on nickel foam as efficient bifunctional electrocatalysts for overall water splitting, *ACS Catal.* 6 (2015) 714–721, <https://doi.org/10.1021/acscatal.5b02193>.
 - [44] S. Yun, H. Zhang, H. Pu, J. Chen, A. Hagfeldt, T. Ma, Metal oxide/carbide/carbon nanocomposites: in situ synthesis, characterization, calculation, and their application as an efficient counter electrode catalyst for dye-sensitized solar cells, *Adv. Energy Mater.* 3 (2013) 1407–1412, <https://doi.org/10.1002/aenm.201300242>.
 - [45] F. Han, S. Yun, J. Shi, Y. Zhang, Y. Si, C. Wang, N. Zafar, J. Li, X. Qiao, Efficient dual-function catalysts for triiodide reduction reaction and hydrogen evolution reaction using unique 3D network aloe waste-derived carbon-supported molybdenum-based bimetallic oxide nanohybrids, *Appl. Catal. B: Environ.* 273 (2020), 119004, <https://doi.org/10.1016/j.apcatb.2020.119004>.
 - [46] C. Wang, S. Yun, Q. Fan, Z. Wang, Y. Zhang, F. Han, Y. Si, A. Hagfeldt, A hybrid niobium-based oxide with bio-based porous carbon as an efficient electrocatalyst in photovoltaics: a general strategy for understanding the catalytic mechanism, *J. Mater. Chem. A* 7 (2019) 14864–14875, <https://doi.org/10.1039/c9ta03540k>.
 - [47] S. Yun, A. Hagfeldt, T. Ma, Superior catalytic activity of sub-5 μm-thick Pt/SiC films as counter electrodes for dye-sensitized solar cells, *ChemCatChem* 6 (2014) 1584–1588, <https://doi.org/10.1002/cctc.201402003>.
 - [48] M.-H. Yeh, S.-H. Chang, L.-Y. Lin, H.-L. Chou, R. Vittal, B.-J. Hwang, K.-C. Ho, Size effects of platinum nanoparticles on the electrocatalytic ability of the counter electrode in dye-sensitized solar cells, *Nano Energy* 17 (2015) 241–253, <https://doi.org/10.1016/j.nanoen.2015.08.008>.
 - [49] S. Yun, H. Pu, J. Chen, A. Hagfeldt, T. Ma, Enhanced performance of supported HfO₂ counter electrodes for redox couples used in dye-sensitized solar cells, *ChemSusChem* 7 (2014) 442–450, <https://doi.org/10.1002/cssc.201301140>.
 - [50] S. Yun, H. Zhou, L. Wang, H. Zhang, T. Ma, Economical hafnium oxygen nitride binary/ternary nanocomposite counter electrode catalysts for high-efficiency dye-sensitized solar cells, *J. Mater. Chem. A* 1 (2013) 1341–1348, <https://doi.org/10.1039/c2ta00680d>.
 - [51] F. Han, S. Yun, J. Shi, Y. Zhang, Y. Si, C. Wang, N. Zafar, J. Li, X. Qiao, Efficient dual-function catalysts for triiodide reduction reaction and hydrogen evolution

- reaction using unique 3D network aloe waste-derived carbon-supported molybdenum-based bimetallic oxide nanohybrids, *Appl. Catal. B: Environ.* 273 (2020), 119004, <https://doi.org/10.1016/j.apcatb.2020.119004>.
- [52] S. Yun, Y. Si, J. Shi, T. Zhang, Y. Hou, H. Liu, S. Meng, A. Hagfeldt, Electronic structures and catalytic activities of niobium oxides as electrocatalysts in liquid-junction photovoltaic devices, *Sol. RRL* 4 (2020), 1900430, <https://doi.org/10.1002/solr.201900430>.
- [53] Y.-Z. Chen, C. Wang, Z.-Y. Wu, Y. Xiong, Q. Xu, S.-H. Yu, H.-L. Jiang, From bimetallic metal-organic framework to porous carbon: high surface area and multicomponent active dopants for excellent electrocatalysis, *Adv. Mater.* 27 (2015) 5010–5016, <https://doi.org/10.1002/adma.201502315>.
- [54] J. Zhu, W. Li, S. Li, J. Zhang, H. Zhou, C. Zhang, J. Zhang, S. Mu, Defective N/S-codoped 3d cheese-like porous carbon nanomaterial toward efficient oxygen reduction and Zn–air batteries, *Small* 14 (2018), 1800563, <https://doi.org/10.1002/smll.201800563>.
- [55] Y. Hou, D. Wang, X.H. Yang, W.Q. Fang, B. Zhang, H.F. Wang, G.Z. Lu, P. Hu, H. J. Zhao, H.G. Yang, Rational screening low-cost counter electrodes for dye-sensitized solar cells, *Nat. Commun.* 4 (2013) 1583, <https://doi.org/10.1038/ncomms2547>.
- [56] X. Zheng, J. Deng, N. Wang, D. Deng, W.-H. Zhang, X. Bao, C. Li, Podlike N-doped carbon nanotubes encapsulating feni alloy nanoparticles: high-performance counter electrode materials for dye-sensitized solar cells, *Angew. Chem. Int. Ed.* 53 (2014) 7023–7027, <https://doi.org/10.1002/anie.201400388>.
- [57] D. Chen, R. Lu, R. Yu, Y. Dai, H. Zhao, D. Wu, P. Wang, J. Zhu, Z. Pu, L. Chen, J. Yu, S. Mu, Work-function-induced interfacial built-in electric fields in Os-OsSe₂ heterostructures for active acidic and alkaline hydrogen evolution, *Angew. Chem. Int. Ed.* 61 (2022), e202208642, <https://doi.org/10.1002/anie.202208642>.
- [58] C. Zhang, R. Du, J.J. Biendicho, M. Yi, K. Xiao, D. Yang, T. Zhang, X. Wang, J. Arbiol, J. Llorca, Y. Zhou, J.R. Morante, A. Cabot, Tubular CoFeP@CN as a Mott–Schottky catalyst with multiple adsorption sites for robust lithium–sulfur batteries, *Adv. Energy Mater.* 11 (2021), 2100432, <https://doi.org/10.1002/aenm.202100432>.
- [59] Z. Zhuang, Y. Li, Z. Li, F. Lv, Z. Lang, K. Zhao, L. Zhou, L. Moskalova, S. Guo, L. Mai, MoB/g-C₃N₄ interface materials as a schottky catalyst to boost hydrogen evolution, *Angew. Chem. Int. Ed.* 57 (2018) 496–500, <https://doi.org/10.1002/anie.201708748>.
- [60] J. Wang, Q. Wei, Q. Ma, Z. Guo, F. Qin, Z.R. Ismagilov, W. Shen, Constructing Co@N-doped graphene shell catalyst via Mott-Schottky effect for selective hydrogenation of 5-hydroxymethylfurfural, *Appl. Catal. B: Environ.* 263 (2020), 118339, <https://doi.org/10.1016/j.apcatb.2019.118339>.
- [61] R. Wang, M. He, Y. Zhou, S. Nie, Y. Wang, W. Liu, Q. He, W. Wu, X. Bu, X. Yang, Metal–organic frameworks self-templated cubic hollow Co/N/C@MnO₂ composites for electromagnetic wave absorption, *Carbon* 156 (2020) 378–388, <https://doi.org/10.1016/j.carbon.2019.09.063>.
- [62] M. Li, Y. Zhu, H. Wang, C. Wang, N. Pinna, X. Lu, Ni strongly coupled with Mo₂C encapsulated in nitrogen-doped carbon nanofibers as robust bifunctional catalyst for overall water splitting, *Adv. Energy Mater.* 9 (2019), 1803185, <https://doi.org/10.1002/aenm.201803185>.
- [63] Y. Ma, M. Chen, H. Geng, H. Dong, P. Wu, X. Li, G. Guan, T. Wang, Synergistically tuning electronic structure of porous β -Mo₂C spheres by Co doping and Mo-vacancies defect engineering for optimizing hydrogen evolution reaction activity, *Adv. Funct. Mater.* 30 (2020), 2000561, <https://doi.org/10.1002/adfm.202000561>.